Doubly-resonant two-photon-absorption-induced four-wave mixing in Tb(OH)3 and LiTbF4
by David Adams Ender

A thesis submitted in partial fulfillment of the requirements for the degree of DOCTOR OF PHILOSOPHY in Physics
Montana State University

Abstract:
Doubly-resonant two-photon-absorption-induced four-wave mixing has been observed for the first time in a rare earth insulator. The generation of the nonlinear signal exhibits strong intermediate and two-photon resonances in crystalline Tb (OH)3 and LiTbF4 This provides a novel method for high resolution measurements of intermediate 4f^n configurations and excited configurations of rare earth ions.

The intermediate resonance showed spectral line narrowing up to ten times narrower than the corresponding inhomogeneously broadened absorption. In LiTbF4, laser-limited line widths were obtained and in Tb(OH)3, a homogeneous limit corresponding to T2 = 50 psec may have been reached. The qualitative behavior of the narrowing is explained by the dispersion of the anamalous index of refraction and its effect on phase matching. Direct measurement of the anamalous dispersion was made to test the model. Results indicate nonlinear contributions to the refractive index may have been present.

The two-photon resonance in Tb(OH)3 was measured to be a 230 cm^-1 wide crystal field component of the broad 4f^n 5d excited configuration. Thus high resolution UV spectroscopy with tunable visible lasers is demonstrated.

Applications are discussed including the extraction of homogeneous line widths from inhomogeneously broadened spectra, coherent transient measurements, and UV and VUV spectrosocpy. The latter uses different selection rules than linear absorption methods and allows study of transitions between excited states.

DOUBLY-RESONANT TWO-PHOTON-ABSORPTION-INDUCED FOUR-WAVE MIXING IN $Tb(OH)_3$ AND $LiTbF_4$

by

DAVID ADAMS ENDER

A thesis submitted in partial fulfillment
of the requirements for the degree

of

DOCTOR OF PHILOSOPHY

in

Physics

Approved:

R L Cone
Chairperson, Graduate Committee

Head, Major Department

Michael Malone
Graduate Dean

MONTANA STATE UNIVERSITY
Bozeman, Montana

August, 1982

ACKNOWLEDGEMENTS

The author wishes to acknowledge the contributions of several people to the preparation of this thesis. Foremost has been the encouragement and patience of his adviser, Dr. R. L. Cone, who initiated the project and whose scientific knowledge and guidance helped bring it to completion.

Thanks also are due to Mr. Michael Otteson and Ms. Paula Fisher for help in building equipment and computerization; to Mr. Tony Knick, Mr. Al Beldring, and Mr. Mark Baldwin in building apparatus; to Mr. Milt Jaehnig for his help in leak detection; to Dr. Roy Wiegand for his successful efforts at keeping the liquid nitrogen machine working; to Dr. Douglas Jones for the laser trigger and delay unit; and to Mr. Mark Ritter for sample preparation.

The author also wishes to thank the members of his committee for their encouragement and suggestions.

He thanks the National Science Foundation for its support as well as the Research Corporation.

Finally, he wishes to extend heartfelt thanks to his parents for their encouragement over the years.

TABLE OF CONTENTS

LIST OF TABLES

LIST OF FIGURES

List of Figures, Continued

Abstract

Doubly-resonant two-photon-absorption-induced four-wave mixing has been observed for the first time in a rare earth insulator. The generation of the nonlinear signal exhibits strong intermediate and two-photon resonances in crystalline $Tb(OH)_3$ and $LiTbF_4$. This provides a novel method for high resolution measurements of intermediate $4f^n$ configurations and excited configurations of rare earth ions.

The intermediate resonance showed spectral line narrowing up to ten times narrower than the corresponding inhomogeneously broadened absorption. In $LiTbF_4$, laser-limited line widths were obtained and in $Tb(OH)_3$, a homogeneous limit corresponding to $T_2 = 50$ psec may have been reached. The qualitative behavior of the narrowing is explained by the dispersion of the anamalous index of refraction and its effect on phase matching. Direct measurement of the anamalous dispersion was made to test the model. Results indicate nonlinear contributions to the refractive index may have been present.

The two-photon resonance in $Tb(OH)_3$ was measured to be a 230 cm^{-1} wide crystal field component of the broad $4f^n5d$ excited configuration. Thus high resolution UV spectroscopy with tunable visible lasers is demonstrated.

Applications are discussed including the extraction of homogeneous line widths from inhomogeneously broadened spectra, coherent transient measurements, and UV and VUV spectrosocpy. The latter uses different selection rules than linear absorption methods and allows study of transitions between excited states.

Chapter 1

HISTORY AND SURVEY

The propagation of an intense laser beam in matter often generates light at frequencies different than that of the laser itself. Several laser beams can create light at a mixture of frequencies. In addition, such light mixing can interact coherently with the medium of propagation as well as exhibit resonant behavior. The branch of optics describing these phenomena is called nonlinear optics.

The subject of this thesis deals with the first observation of two nonlinear optical effects: (1) doubly-resonant two-photon absorption-induced four-wave mixing (TPAFWM) in rare earth insulators (specifically $Tb(OH)_3$ and $LiTbF_4$), and (2) phase matching induced line narrowing.

The initial observation of the TPAFWM signal was made by Rufus Cone and Joel Friedman at Bell Telephone Laboratories, Murray Hill.[1] Light at $\omega_4 = \omega_1 + \omega_2 - \omega_3$ was observed upon application of beams at frequencies ω_1, ω_2 and ω_3. The ω_4 beam intensity exhibits resonant behavior as the input beams are tuned relative to transitions of the crystal, making this technique highly useful for spectroscopy.

The surprising thing found at Murray Hill was the extreme spectral narrowing exhibited by the ω_4 signal

inside the corresponding ω_1 absorption line shape (see Figure 1.1). Subsequent observations at Montana State University showed that the narrowed line could be driven from one side of the ω_1 resonance to the other upon variation of the beam crossing angles.[2] This report confirms this as a TPAFWM process and explains the nature of the narrowing, the peculiar shape, and its spectral motion. Utilization of this process as a spectroscopic tool will also be discussed.[3]

History

The field of nonlinear optics was ushered in by the classic experiment done in July of 1961 by Franken, Hill, Peters, and Weinreich[4] in which second harmonic generation (SHG) was first measured. Light from a ruby laser at 6943 Å was focused into a crystalline quartz sample as in Figure 1.2. The resultant beam was spectrally analyzed yielding photographic plates showing not only light at 6943 A but also a faint spot at 3471.5 Å. The conversion efficiency was 10^{-8}. Today, efficiencies close to one are routinely achieved.[5]

Nonlinear optical effects arise from higher order terms of the induced polarization of a medium which is

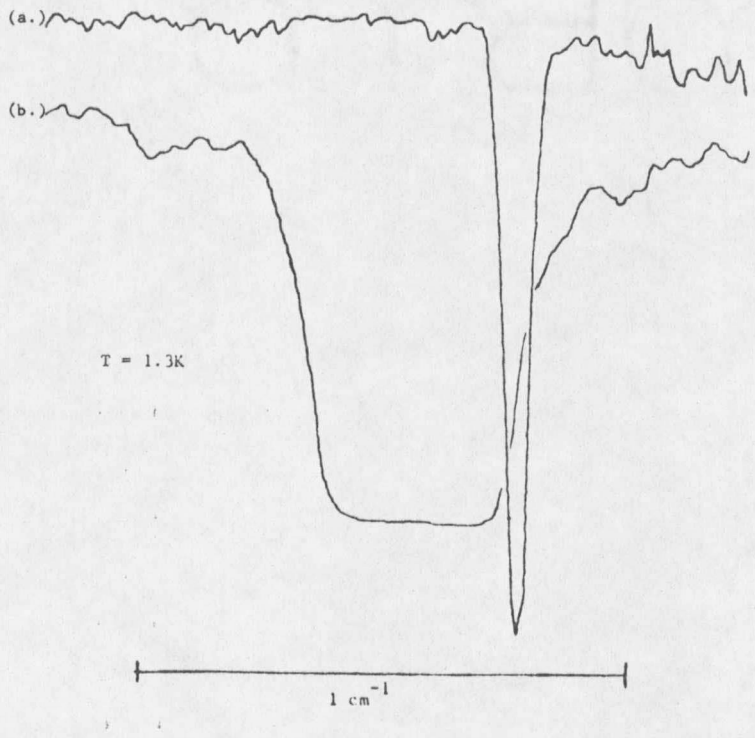

Figure 1.1.(a.) Four-wave mixing signal, and (b.) corresponding absorption for the $^5D_4\Gamma_1$ state of $LiTbF_4$. ω_3 = 17422 cm^{-1}. Crossing angle θ = 1.50°.

written as an expansion in powers of E/E_{at}:

$$P = \chi E(1 + C_1 \frac{E}{E_{at}} + C_2 (\frac{E}{E_{at}})^2 + \ldots) \qquad (1.1)$$

The C_i are expansion coefficients of order one and $E_{at} \sim \frac{e}{a_o^2} = 1.7 \times 10^7$ statvolts/cm is the typical atomic field an electron sees in a transparent insulator (a_o = one Bohr radius).

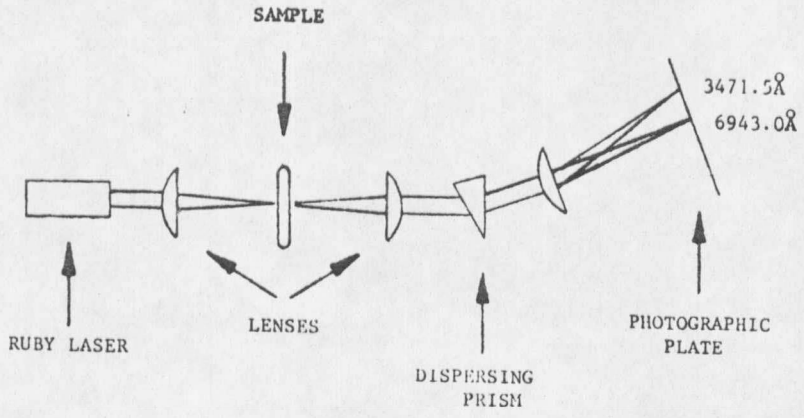

Figure 1.2. Second harmonic generation in crystalline quartz. The ruby laser emits at 6943.0Å. The sample generates light at 3471.5Å.

This oscillating polarization acts as a source term in Maxwell's equations generating light at the various frequencies given by a Fourier decomposition of P.

One usually rewrites Equation (1.1) as

$$\vec{P} = \varepsilon_0 \chi^{(1)} \cdot \vec{E} + \chi^{(2)} : \vec{E}\vec{E} + \chi^{(3)} \vdots \vec{E}\vec{E}\vec{E} + \ldots, \qquad (1.2)$$

where the tensor coefficients of the electric field are referred to as the linear ($\chi^{(1)}$) and nonlinear ($\chi^{(2)}$, $\chi^{(3)}$, ...) electric susceptibilities of the medium.

We can see immediately that the oscillation of the parent electric field at frequency ω in Franken's SHG

experiment will generate a polarization in the medium oscillating at 2ω for nonzero $\chi^{(2)}$. Likewise, higher order terms will produce other harmonics and for situations involving input waves of distinct frequencies various sum and difference frequencies will be generated. Nonlinear optics is a colorful subject.

Nonlinear effects in the polarization have been studied since the nineteenth century (Pockels and Kerr effects).[6] However, it wasn't until the advent of the laser in July of 1960 that the ability was obtained to generate light waves intense enough to utilize the higher order terms in the expanded polarization.[7]

Consequently, little motivation existed to develop a global theoretical approach to the many nonlinear optical effects awaiting discovery. The years from 1961 to the present have been spent primarily laying the theoretical framework, fitting new observations into it, and working out the finer details of the theory.

While the future still holds promise for the discovery of new effects, the majority of workers in the field are directing their research more toward device applications[8] or applications of nonlinear optical spectroscopy. The latter topic is considered important enough that Nicholaas

Bloembergen and Arthur Schawlow won the 1981 Nobel prize in physics for their work in the field.[9] In particular, it is Bloembergen's work in four-wave mixing that forms the background for this thesis.

Nonlinear Spectroscopy

Several general reviews exist on the field of nonlinear optical spectroscopy. Bloembergen has written several excellent articles on nonlinear optics for which two are exceptionally comprehensive.[10] Hänsch,[11] Levenson,[12] and Brewer[13] each have short topical articles with good reference lists on some of the more important subfields on nonlinear optical spectoscopy. More recent reviews are given by Levenson and Song[14] and Laubereau and Kaiser[15] on coherent Raman spectroscopy and coherent time domain Raman spectroscopy respectively. The former is worthwhile on the basis of its reference list alone.

Nonlinear laser spectroscopy provides information in both frequency and temporal domains. In many cases it offers distinct advantages over linear spectroscopy. These include higher resolution and signal sensitivity. Dynamics of collective excitations, both coherent and incoherent, can be studied, and multiphoton processes enable different

sets of selection rules to be used.

Frequency Domain Spectroscopy

Many methods have been developed for spectroscopy in the frequency domain. Use of the third order susceptibility $\chi^{(3)}$ provides such techniques as stimulated Raman scattering (SRS),[14,16,17] coherent antistokes Raman spectroscopy (CARS),[12,14,18] coherent Stokes Raman spectroscopy (CSRS),[19,20] two-photon-absorption-induced four-wave mixing (TPAFWM),[21,22,23] and degenerate four-wave mixing (DFWM).[24,25,26] A chief advantage of these techniques lies in the fact that the output signal is generally separated spatially from the input beams and is of a different frequency. Thus easy signal discrimination is obtained.

The ability to measure homogeneous linewidths inside of inhomogeneously broadened[27] spectral lines is a topic of much interest. By measuring the width of the homogeneous line one obtains the associated relaxation time. This provides insight into the dynamics of the excited state. Certain nonlinear techniques can extract this information where linear techniques fail.

One such method, saturation or hole-burning spectroscopy,[28,29] involves saturating the narrower homogeneous

part of the inhomogeneous line with a strong pump laser, then probing the absorption profile with a weaker probe beam. When the probe frequency comes into the saturated part of the absorption, it is no longer absorbed. Thus, an absorption profile with a "hole" is mapped out. The hole provides a measure of the homogeneous linewidth.

Doppler-free two-photon spectroscopy[11,30] complements single photon spectroscopy in that it provides spectral information between states of the same parity. It is especially valuable in studying gases where the photon frequencies are Doppler shifted as viewed by molecules traveling with different velocities. This inhomogeneously broadens the transition. By utilizing photons traveling in opposite directions, the first order Doppler shifts cancel yielding nearly homogeneous line shapes in the fluorescence spectrum.

Nonlinear polarization spectroscopy[11,31,32] is closely related to saturation spectroscopy. However, rather than monitoring the probe's absorption, the polarization is examined. The pump laser induces a birefringence in the sample which changes the polarization of the probe. By placing the sample between crossed polarizers, very high signal-to-noise ratios are possible. When the pump and

probe frequencies differ by a Raman transition, this method is called RIKES (Raman Induced Kerr Effect Spectroscopy).[12,33]

Time Domain Spectroscopy

Nonlinear spectroscopy can also be applied to the time domain, allowing relaxation rates to be measured directly. This is especially useful in those situations where homogeneous linewidths are too narrow to be measured directly with present lasers. These kinds of measurements are called coherent transient techniques[13,34] because they involve inducing a coherent state in the system under study, terminating the source of coherence, and finally probing the relaxation as a function of time.

Two kinds of relaxation processes are distinguished. Those processes that act to destroy the induced collective coherence of the atomic dipoles are called transverse processes and have decay time T_2, while those that depopulate the energy levels are longitudinal processes having decay time T_1. The terminology is borrowed from nuclear magnetic resonance language because a two-level optical system can be described in terms of the Bloch equations.[34]

Free induction decay and photon echo experiments

provide means to measure the homogeneous T_2 of inhomogeneously broadened lines.[35] Macfarlane and Shelby,[36] using a photon echo technique, have been able to measure T_2 of 429 μsec corresponding to a homogeneous linewidth of 760 Hz in $Eu^{3+}:Y_2O_3$. This is the smallest homogeneous linewidth ever measured.

A different approach to measuring relaxation times involves delayed probing of a coherently prepared system. CARS,[37,38] TPAFWM, and other multi-beam techniques can be used as time domain methods by temporal sequencing of the pulses from different lasers. Induced coherence established by earlier pulses decays away upon pulse termination. Sampling of the remaining coherence as a function of the delay time of a later proble pulse allows T_2 to be measured. In addition, the delayed CARS technique can also be used to measure T_1.[37]

The above survey of experimental methods is by no means intended to be complete, but rather is meant to give the reader a flavor for the many ways in which nonlinear optical techniques can be used in spectroscopy. One of the methods mentioned, two-photon-absorption-induced four-wave mixing is the thrust of this thesis.

Chapter 2

THEORY OF FOUR-WAVE MIXING IN SOLIDS

The theory of four-wave mixing (FWM) is presented first in order to provide a framework from which to understand the phenomena observed. Then the relevant properties of the materials under study, namely $Tb(OH)_3$ and $LiTbF_4$, are presented. It should be noted, however, that the line narrowing and spectral selectivity observed is a general effect which needs to be considered in resonant FWM experiments on all materials in condensed states. This will become apparent in Chapter 4.

Four-Wave Mixing

The fitting of new observations into the theoretical framework of nonlinear optics requires examination of the underlying assumptions made. Furthermore, as will be seen, the nonlinear susceptibility is composed of several terms, each describing a different nonlinear process. In order to understand the nature of the signal observed, investigation of the contribution of these terms is necessary. The following treatment, taken from Ducuing and from Bloembergen[39], highlights both the assumptions made and relevant terms needed to explain our observations.

Four-wave mixing is treated most suitably using a semiclassical approach which treats the light fields classically and the material quantum mechanically. Because this is a coherent process, phase information is important and is handled quite conveniently by classical fields. This approach is well justified when dealing with large numbers of photons (i.e. for pulse energies $>> \hbar\omega \sim 4 \times 10^{-19}$ J) as is the case in our experiments.

The strategy is summarized as follows. We are interested in the interaction of Tb^{3+} ions in a crystal with an applied electromagnetic field due to the light. The Hamiltonian is given by $H = H_o + H'(t)$ where H_o is the material Hamiltonian. $H'(t)$ is the perturbation due to the applied field. We use H in the equation of motion for ρ, the quantum mechanical density operator, which is solved by an iterative perturbation technique in which ρ is expanded in powers of H'. The macroscopic polarization of the medium due to H' is given by

$$\vec{P} = N < \vec{\mu} > = N \text{ Trace } (\rho\vec{\mu}) \qquad (2.1)$$

where N = the particle density and $\vec{\mu}$ = the atomic electric dipole moment. Substitution of $\vec{P}$ into Maxwell's equations yields the equation of propagation for $\vec{E}_{rad}(\vec{x},t)$, the gen-

erated wave in the medium. The FWM signal is one of the Fourier components of this wave.

We begin by writing the electric field of the light wave with four frequency components as

$$\vec{E}(\vec{x},t) = \sum_{n=1}^{4} \vec{E}_{on}(\vec{x}) \exp(i\omega_n t) + c.c. \qquad (2.2)$$

The electric dipole approximation is used in which the wavelength of the exciting radiation is long compared to the size of the atom. The Hamiltonian is written

$$H = H_o - e\vec{E}(\vec{x},t) \cdot \vec{x} \qquad (2.3)$$

The equation of motion for ρ in the Schrodinger picture is given by

$$i\hbar\dot{\rho} = [H,\rho] + i\hbar\dot{\rho}_{relax} \qquad (2.4)$$

where $\dot{\rho}_{relax}$ [22] is a phenomenological term included to account for damping of the material resonances. We use basis states $|\ n\ \rangle$ in which H_o is diagonal in writing

$$(\dot{\rho}_{relax})_{nn'} = -\Gamma_{nn'}\rho_{nn'} \qquad (2.5)$$

where $\Gamma_{nn'} = \Gamma_{n'n}$ is the damping constant of the induced dipole moment associated with the states n and n', and

$$(\dot{\rho}_{relax})_{nn} = -\sum_{n'} \gamma_{n'n}\, \rho_{nn} + \sum_{n'} \gamma_{nn'}\, \rho_{n'n'} \qquad (2.6)$$

where $\gamma_{n'n}$ is the transition rate from the state n to n', $T_2 = (2\pi\Gamma_{nn'})^{-1}$ is the dephasing time, and for a two-level system, $T_1 = (\gamma_{n'n})^{-1}$ is the population relaxation time. (Note that it is common in the literature to use "Γ" for dipole decay and "γ" for population decay.)

Expansion of ρ in increasing powers of $H'(t)$ gives, upon substitution into equation (2.4),

$$i\hbar\dot{\rho}^{(n)} = [H_o, \rho^{(n)}] + i\hbar\dot{\rho}^{(n)}_{relax} + [H', \rho^{(n-1)}] \qquad (2.7)$$

where $\rho(t) = \rho^{(0)} + \rho^{(1)} + \rho^{(2)} + \rho^{(3)} + \ldots$ (2.8)

and $\rho^{(0)}(t) = \rho(0)$ defined by the initial conditions that $\rho_{nn}(0)$ equals the thermalized occupation probabilities of the states $|n\rangle$ and $\rho_{nn'}(0) = 0$. At low temperatures this can be further simplified by allowing initial occupation of only the ground state. As discussed in Chapter 4, in our system changes in population are ignored so that $\rho_{gg}(t) = \rho_{gg}(0) = 1$. Finally we look at only the steady state response of $\rho(t)$. This is justified for rapid dephasing ($1/\Gamma_{nn'} \ll$ laser pulse duration) of all dipole moments, which is expected in the concentrated magnetic compounds

under study.

Using (2.1) with the above assumptions we concentrate on the terms in the polarization oscillating at frequency $\omega_4 = \omega_1 + \omega_2 - \omega_3$. Laser frequencies ω_1, ω_2, and ω_3 are chosen for our experiment to match the energy levels as shown in Figure 2.1a.

Defining $\chi^{(3)}$ as in (1.2), we arrive at the following expression[23,39] for $\chi^{(3)}$ applied to our system

$$\chi^{(3)}_{\mu\alpha\beta\gamma}(\omega_4=\omega_1+\omega_2-\omega_3) \propto \sum_{n=\text{all states}} \frac{\mu_{\alpha,ab}\mu_{\beta,bc}\mu_{\mu,cn}\mu_{\gamma,na}\,(-\rho^{(0)}_{aa})}{(\omega_{ba}-\omega_1-i\Gamma_{ba})(\omega_{ca}-(\omega_1+\omega_2)-i\Gamma_{ca})(\omega_{cn}-\omega_4-i\omega_{cn})}$$

$$+ \sum_{n=\text{all states}} \frac{\mu_{\alpha,ab}\mu_{\beta,bc}\mu_{\gamma,cn}\mu_{\mu,na}\,(\rho^{(0)}_{aa})}{(\omega_{ba}-\omega_1-i\Gamma_{ba})(\omega_{ca}-(\omega_1+\omega_2)-i\Gamma_{ca})(\omega_{na}-\omega_4-i\Gamma_{na})} + \quad (2.10)$$

46 other nonresonant (N.R.) terms, where $\omega_{ij} \equiv (E_i-E_j)/\hbar$. Nonresonant terms refer to those terms which are small compared to those shown by choice of the input frequencies ω_1, ω_2, and ω_3.

As discussed in Chapter 4, consideration of Raman contributions such as CARS and CSRS (pronounced "scissors") was necessary. These terms look like[19]

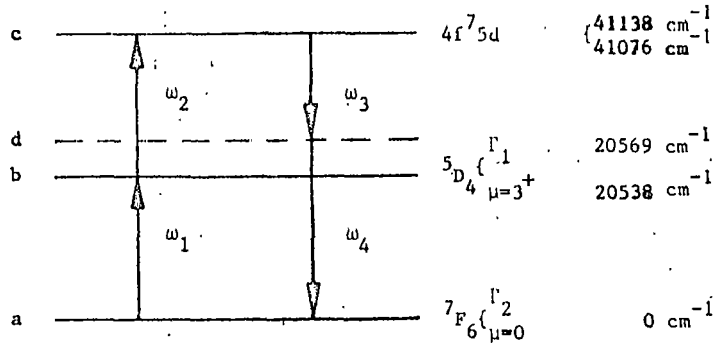

(a.) TPA

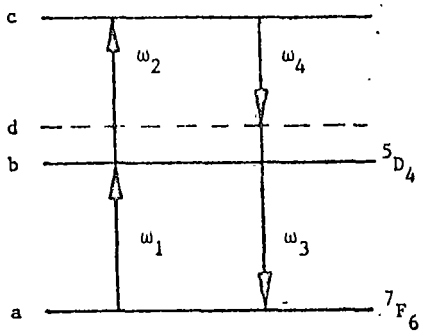

(b.) TPA

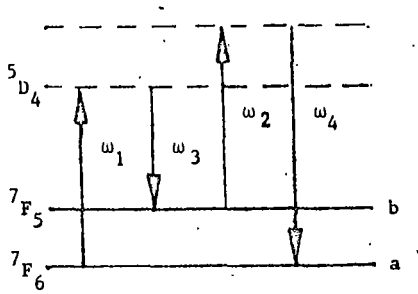

(c.) CARS

Figure 2.1. Energy level diagrams for various terms in $\chi^{(3)}(\omega_4=\omega_1+\omega_2-\omega_3)$. Material energy levels used in our experiments are identified for $\{^{LiTbF_4}_{Tb(OH)_3}$ in Figure (a.).

$$\chi^{(3)}(\omega_4) \sim \frac{1}{(\omega_{ba}-(\omega_1-\omega_3)-i\Gamma_{ba})} \text{ for } \omega_1>\omega_3 \text{ (CARS)} \quad (2.11)$$

$$\sim \frac{1}{(\omega_{ba}+(\omega_1-\omega_3)-i\Gamma_{ba})} \text{ for } \omega_1<\omega_3 \text{ (CSRS)} \quad (2.12)$$

It will be shown later that the signal produced at ω_4 is $\propto |\chi^{(3)}|^2$. Thus interferences can occur between the terms. For this reason it was necessary to know if the Raman terms of (2.11) and 2.12) were contributing resonantly to the signal. We found the ω_4 signal to be independent of $(\omega_1 - \omega_3)$ which tells us that these terms can be relegated to nonresonant status.

For our experiment, we can rewrite (2.10) in a more abbreviated form. Since our chief interest is in scanning ω_1 through state $|b\rangle$, ω_2 and ω_3 are constant and ω_4 is approximately constant relative to any resonances for small change in ω_1. Therefore

$$\chi^{(3)}_{\mu\alpha\beta\gamma}(\omega_4) \propto \frac{A_{\mu\alpha\beta\gamma}}{(\omega_{ba}-\omega_1-i\Gamma_{ba})(\omega_{ca}-(\omega_1+\omega_2)-i\Gamma_{ca})} + \chi^{(3)}_{NR} \quad (2.13)$$

where A is a constant containing the electric dipole matrix elements and factored sums of (2.10).

At this point, mention should be made of local field effects. $\vec{E}$ used in the Hamiltonian of (2.3) is the

microscopic field $\vec{E}_{loc}(\vec{r},t)$. This is equal to the microscopic field felt by the ion minus the field of the ion itself. It includes the light field plus all contributions from the charges in the medium and is highly sensitive to changes in position of neighboring ions. The macroscopic source polarization $\vec{P}$ used in Maxwell's equations is defined using the macroscopic field $\vec{E}(\vec{r},t)$. In order to amend the situation, a correction factor[40] is inserted in the polarization which contains polynomials of $\varepsilon(\omega)$, where ε is the dielectric tensor. This could be a significant effect in certain cases in which additional resonant behavior could manifest itself. The tensor nature of ε also complicates things.

As discussed in Chapter 4, the spectral line narrowing is found to be dependent on parameters other than resonant behavior in the local field correction factor. Furthermore, all input beams are kept within small angles of the surface normal to the crystal. For uniaxial crystals with high symmetry, such as those used in our experiments, these small angles are unimportant so we shall ignore the correction factor in subsequent discussion.

Now that we know how the medium responds to the field $\vec{E}$ through $\chi^{(3)}$, we are in a position to calculate the equation of propagation of the light through the crystal. The approach taken is generalized from Yariv.[41] We start with the following experimental situation.

We have an absorbing crystal in which we are propagating three laser beams of different frequencies, all approximately along the $\hat{x}$ direction and intersecting at small angles just inside the crystal surface. We assume traveling plane waves for the light fields and write for the total electric field in the interaction region inside the crystal

$$E_i(x,t) = \sum_{n=1}^{4} E_i^n(x,t) \tag{2.14}$$

where $$E_i^n(x,t) = \frac{1}{2}[E_{ni}(x)e^{i(\omega_n t - \vec{K}_n \cdot \vec{x})} + c.c.] \tag{2.15}$$

Four fields in (2.14) have been included to allow for the nonlinear generation of light at our signal frequency ω_4. The subscript i gives the polarization, $\hat{z}$ or $\hat{y}$.

These fields generate a polarization in the medium which acts as a source term in Maxwell's wave equation

$$\frac{\partial^2}{\partial x^2}\vec{E} = \mu_o\sigma\frac{\partial\vec{E}}{\partial t} + \mu_o\varepsilon_o\frac{\partial^2\vec{E}}{\partial t^2} + \mu_o\frac{\partial^2}{\partial t^2}\vec{P}. \qquad (2.16)$$

The polarization $\vec{P}$ can be written as the sum of a linear and nonlinear part such that

$$\vec{P} = \varepsilon_o\chi_1\vec{E} + \vec{P}_{NL} \qquad (2.17)$$

where χ_1 is the linear electric susceptibility and, using the Einstein summation convention,

$$(P_{NL})_i = \chi^{(2)}_{ijk}\ E_jE_k + \chi^{(3)}_{ijk\ell}\ E_jE_kE_\ell + \ldots \qquad (2.18)$$

We are interested in only those Fourier components of $\vec{P}$ that drive the wave equation at $\omega_4 = \omega_1 + \omega_2 - \omega_3$, the frequency at which our signal occurs. Inserting $\vec{P}_{NL}(\omega_4)$ into (2.16) we find the field amplitudes (2.15) obey

$$\frac{dE_{1j}}{dx} = \frac{-\sigma_1}{2}\sqrt{\frac{\mu_o}{\varepsilon_1}}\,E_{1j} - \frac{3}{4}i\omega_1^2\,\mu_o\chi^{(3)}_{jk\ell i}E^*_{2k}E_{3\ell}E_{4i}\,\exp[-i(\Delta\vec{k})_1\cdot\vec{x}]/k_1$$

$$\frac{dE_{2k}}{dx} = \frac{-\sigma_2}{2}\sqrt{\frac{\mu_o}{\varepsilon_2}}\,E_{2k} - \frac{3}{4}i\omega_2^2\mu_o\chi^{(3)}_{k\ell ij}E_{3\ell}E_{4i}E^*_{1j}\,\exp[-i(\Delta\vec{k})_2\cdot\vec{x}]/k_2$$

$$\frac{dE_{3\ell}}{dx} = \frac{-\sigma_3}{2}\sqrt{\frac{\mu_o}{\varepsilon_3}}\,E_{3\ell} - \frac{3}{4}i\omega_3^2\mu_o\chi^{(3)}_{\ell ijk}E^*_{4i}E_{\ell j}E_{2k}\,\exp[-i(\Delta\vec{k})_3\cdot\vec{x}]/k_3$$

$$\frac{dE_{4i}}{dx} = \frac{-\sigma_4}{2}\sqrt{\frac{\mu_o}{\varepsilon_4}}E_{4i} - \frac{3}{4}i\omega_4^2\mu_o\chi^{(3)}_{ijk\ell}E_{1j}E_{2k}E^*_{3\ell}\exp[-i(\Delta\vec{k})_4\cdot\vec{x}]/k_4 \tag{2.19}$$

where $(\Delta\vec{k})_1 \equiv (\vec{k}_3 + \vec{k}_4 - \vec{k}_2 - \vec{k}_1) = (\Delta\vec{k})_2 = -(\Delta\vec{k}_3) = -(\Delta\vec{k}_4)$

and where the slowly varying amplitude approximation $(\frac{\partial E_{ni}}{\partial x}k_n >> \frac{\partial^2 E_{ni}}{\partial x^2})$ has been used. Subscripts n on σ_1, ε_n, k_n and E_{ni} indicate frequency dependence ω_n.

Equations (2.19) can be uncoupled if we allow beam depletion due to absorption, but not conversion to E_{4i}. Thus we have immediately

$$E_{1j} = E_{1j}(0)e^{-\alpha_1 x/2}$$

$$E_{2k} = E_{2k}(0)e^{-\alpha_2 x/2}$$

$$E_{3\ell} = E_{3\ell}(0)e^{-\alpha_3 x/2} \tag{2.20}$$

where $\alpha_i = \sigma_i\sqrt{\frac{\mu_o}{\varepsilon_i}}$ is the absorption coefficient at frequency ω_i. Setting $\Delta k_4 = \Delta k$ and using (2.20), the last of equations (2.19) can be readily integrated to give

$$E_{4i}(x) = \frac{3}{4}\omega_4\sqrt{\frac{\mu_o}{\varepsilon_4}}\chi^{(3)}_{ijk\ell}E_{ij}(0)E_{2k}(0)E^*_{3\ell}(0)\left(1-e^{-i\Delta\vec{K}\cdot\vec{x}}\right) \times \exp\left(-\alpha_4 x/2\right)/\Delta K \qquad (2.21)$$

where $\Delta\vec{K} \equiv \Delta\vec{k} - i\,\Delta\vec{\alpha}/2$

and $\Delta\vec{\alpha} = (\alpha_1 + \alpha_2 + \alpha_3 - \alpha_4)\hat{x}$ (2.22)

The detected intensity at ω_4 is $\frac{1}{2}(\varepsilon_4/\mu_o)^{\frac{1}{2}}|E_{4i}|^2$ so for an interaction length L the intensity is

$$I_{4i} \propto (L/2)^2\exp(-\alpha_4 L)\left|\chi^{(3)}_{ijk\ell}(\omega_4)E_{1j}(0)E_{2k}(0)E^*_{3\ell}(0)\right|^2 \times G(\Delta K) \qquad (2.23)$$

where $G(\Delta K)$, the phase matching factor, is given by

$$G(\Delta K) = \frac{1+\exp(-\Delta\alpha\ L)-2\exp[-\Delta\alpha\ L/2]\cos(\Delta k\ L)}{(\Delta k^2 + \Delta\alpha^2/4)\left(\frac{L}{2}\right)^2} \qquad (2.24)$$

For samples with inhomogeneously broadened transitions, $\chi^{(3)}$, $\Delta\alpha$ and $n(\omega)$ must be integrated over the entire linewidth. Inhomogeneous broadening will be discussed at the end of the chapter.

Equations (2.13), (2.23), and (2.24) constitute the main results of this section. (See Table 2.1.) They describe the two major effects of interest: resonant behavior and phase matching.

The phase matching factor $G(\Delta K)$ is present because

Table 2.1

Summary of Relevant Equations

$$\chi^{(3)}_{ijk\ell}(\omega_4) \propto \frac{A_{ijk\ell}}{(\omega_{ba} - \omega_1 - i\Gamma_{ba})(\omega_{ca} - (\omega_1 + \omega_2) - i\Gamma_{ca})} + \chi^{(3)}_{NR} \qquad (2.13)$$

where $\omega_4 = \omega_1 + \omega_2 - \omega_2$.

$$\Delta\vec{K} = (\vec{k}_1 + \vec{k}_2 - \vec{k}_3) - \vec{k}_4 \text{ where } k_i = \omega_i n_i / c \qquad (2.19)$$

$$\Delta\alpha = \alpha_1 + \alpha_2 + \alpha_3 - \alpha_4 \qquad (2.22)$$

$$I_{4i} \propto (L/2)^2 \exp(-\alpha L) \left| \chi^{(3)}_{ijk\ell}(\omega_4) E_{1j}(0) E_{2k}(0) E^*_{3\ell}(0) \right|^2 G(\Delta K) \qquad (2.23)$$

$$G(\Delta K) = (1 + \exp(-\Delta\alpha L) - 2 \exp(-\Delta\alpha L/2) \cos(\Delta k L)) / \left[(\Delta k^2 + (\Delta\alpha/2)^2)(L/2)^2 \right] \qquad (2.24)$$

of the coherence of the nonlinear process. High efficiency is maintained only as long as the generated wave (or signal) at ω_4 remains in phase with the driving (or source) polarization throughout the region of interaction. The dispersive character of condensed media precludes phase matching for collinear beams where signal and source waves travel with different phase velocities in the medium. However, by crossing the beams inside the crystal at angles that satisfy $\Delta\vec{k} = 0$, phase matching is achieved and $G(\Delta K)$ is maximized.

A familiar form for $G(\Delta K)$ occurs in the totally nonresonant case ($\alpha_1=\alpha_2=\alpha_3=\alpha_4=0$). Then $G(\Delta K)$ reduces to

$$G(\Delta k) = \frac{\sin^2(\Delta k\, L/2)}{(\Delta k\, L/2)^2} \equiv \mathrm{sinc}^2(\Delta k\, L/2).$$

A graph of $\mathrm{sinc}^2(\Delta k\, L/2)$ appears in Figure 2.2.

Figure 2.3 shows two-beam and three-beam phase matching diagrams. $\Delta\vec{k}$ is the degree to which the figures are unclosed and has a magnitude given by

$$\Delta k_{\perp} = k_3 - (4k_1^2 + k_2^2 - 4k_1k_2 \cos\theta)^{\frac{1}{2}} \qquad (2.25)$$

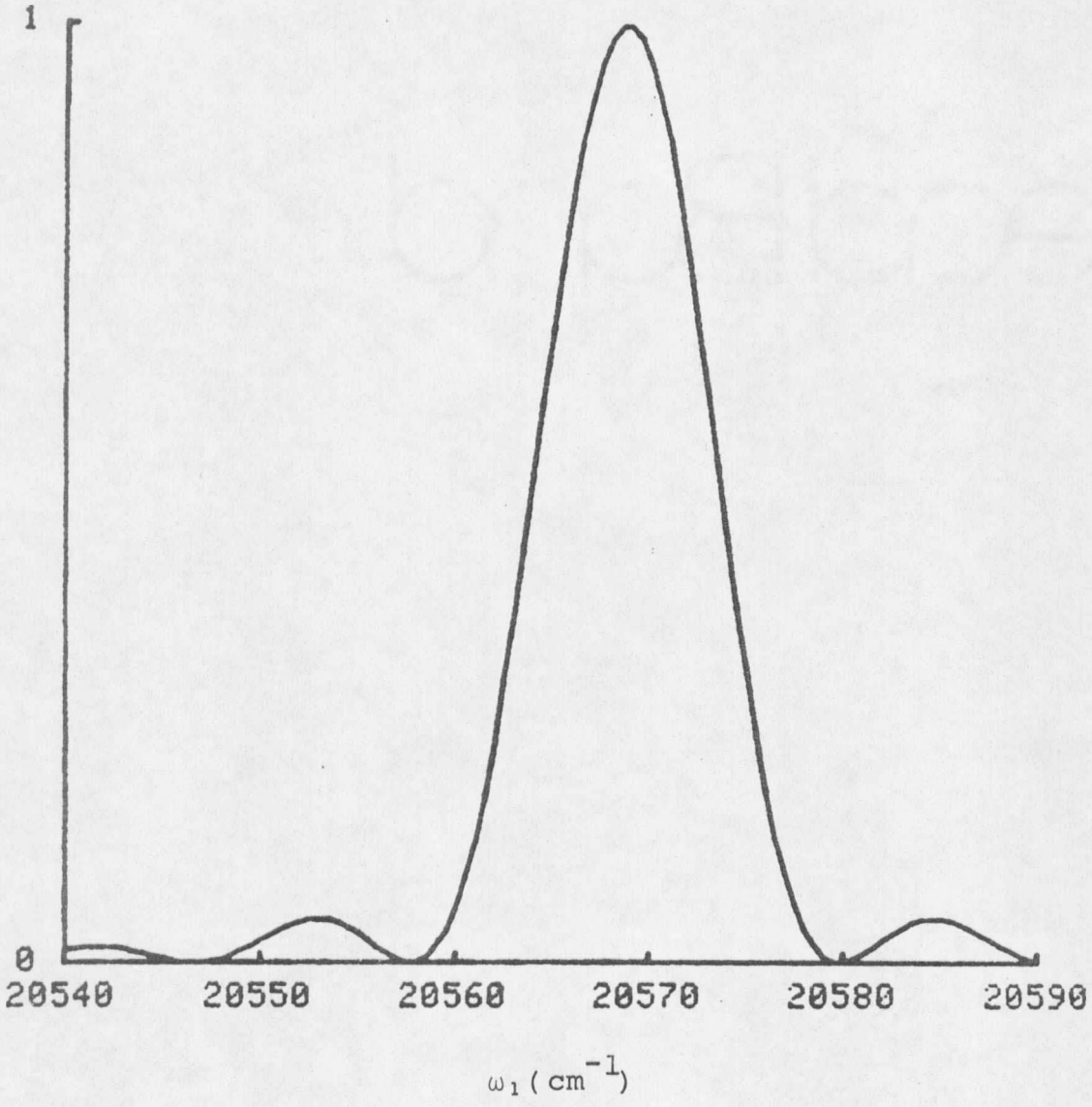

Figure 2.2. $Sinc^2(\Delta k\ L/2)$ vs. ω_1 using parameters in $\Delta k\ L$ relevant to the experiment. These include L = 0.03 cm, n_1 = 1.508, θ = 2.15° and $k_2 = 1.646 \times 10^5 cm^{-1}$.

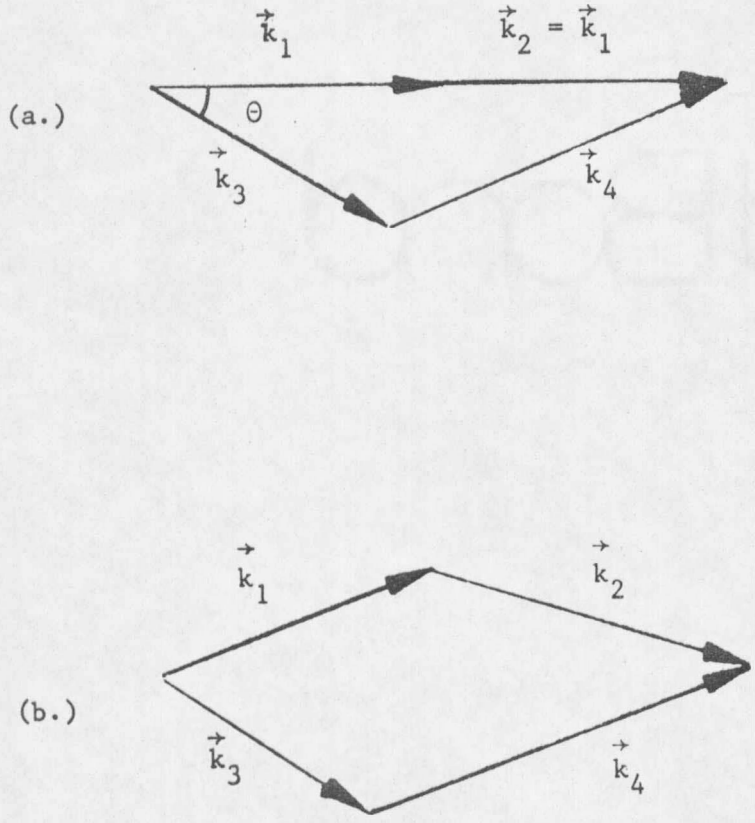

Figure 2.3. Phase matching diagrams showing (a.) 2- beam geometry with beam crossing angle θ, and (b.) the more general 3- beam geometry.

where $k_i = \omega_i n_i / c$. (2.26)

Note that the ω_4 beam (of wavevector $\vec{k}_4$) is directionally distinct from all other beams allowing for easy discrimination of the signal.

Besides phase matching, a second consequence of the nonlinear interaction is the possibility of interference between the nonresonant background signal and the real part of the susceptibility. This arises from $|\chi^{(3)}|^2 = |\chi^{(3)}_{res} + \chi^{(3)}_{NR}|^2$ in (2.23). In most situations, $\chi^{(3)}_{NR}$ is approximately real while $\chi^{(3)}_{res}$ is complex. This gives

$$|\chi^{(3)}|^2 = (\chi^{(3)'}_{NR} + \chi^{(3)'}_{res})^2 + \chi^{(3)''2}_{res}$$

where the prime and double prime refer to real and imaginary parts of $\chi^{(3)}_{res}$ respectively. For significant values of $\chi^{(3)'}_{NR}$, the cross term can give a distinctly anomalous shape to the resonance.[18,42] Therefore, in experiments where lineshape is important, interference must be considered.

Note that the above discussion has completely ignored any consideration of $\chi^{(2)}$. This is justified in centrosymmetric crystals where all even order terms in the $\vec{P}$ expansion vanish due to symmetry considerations. This is not true for noncentrosymmetric systems (our case) and one

may ask whether $\chi^{(2)}$ contributes to the ω_4 signal.

Because the second order term involves only mixing of two light fields, no Fourier components directly appear at ω_4. Such components can arise, however, in a two-step process.[43] First $\chi^{(2)}$ generates light at the frequencies $(\omega_1+\omega_2)$, $(\omega_1-\omega_3)$, and $(\omega_2-\omega_3)$. The light at these frequencies can combine in the second step with the primary beams at $-\omega_3$, $+\omega_2$, and $+\omega_1$ respectively to achieve a signal at $\omega_4 = \omega_1 + \omega_2 - \omega_3$. We show in Chapter 4 that for the beam polarizations used in our experiment, $\chi^{(2)}_{izz} = 0$.

Finally, two assumptions need further elaboration. The first, used in deriving $\chi^{(3)}$ from ρ, involved the assumption of minimal population change from the initial conditions. In cases away from strong resonance, this is satisfactory. However, population dynamics ought to be considered in spectroscopy on strong transitions. We show in Appendix II that population changes are small for our case.

The second assumption was the plane-wave approximation made in solving Maxwell's wave equation. Laser beams are better described by Gaussian beam optics[44] in which the plane-wave approximation is valid only for areas inside the confocal region, b, of the beam focus. In this region, the beam wave fronts are planes; outside they begin to make

the transition to spherical waves. For $\frac{L}{b} \gtrsim 1$, significant changes occur in phase matching and an approach such as that taken by Bjorklund[45] must be used. In our situation, however, $\frac{L}{b} \sim .02$ so that equation (2.23) is valid.

Materials

The active ion used in the experiments was terbium, which was hosted in concentrated form in $Tb(OH)_3$ and $LiTbF_4$. These compounds were chosen for purely pragmatic reasons; it was in $Tb(OH)_3$ that the narrowed FWM resonance was first observed. Initial interest in $Tb(OH)_3$ involved study of exciton dynamics associated with the $^5D_4\ \mu = 2 - {}^7F_5\ \mu = 1$ transition.[46,47] It was on the $^5D_4\ \mu = 3^+$ state that the FWM signal was found. In retrospect the accessibility of energy levels, narrow linewidths, and transparency of the crystal makes these compounds extremely attractive for this kind of spectroscopy. The importance of each of these items will become clear in later chapters.

Several excellent reviews exist on rare earth spectroscopy.[48,49] Much of this section is taken from Dieke[50] and Scott.[51] A cursory description is given here in which only relevant highlights of energy levels and selection

rules are presented. A short section on spectral line broadening is presented at the end.

Rare earths are exceptionally attractive in solid state spectroscopy primarily because of their near atomic-like properties. These properties arise from the spatial contraction of the $4f^n$ radial wave-function known as the lanthanide contraction. For rare earth atoms which have large atomic number, the electronic shielding of the nucleus becomes less effective drawing the 4f electrons well inside the closed 6s, 5p, and 5s shells[50] encouraging very little participation with the environment. Chemical properties are very similar throughout the entire series--bond formation occurs first with the 6s electrons. Furthermore, the static electric field from other ions (known as the crystal field) by the $4f^n$ electrons is reduced to a small perturbation on the atomic Hamiltonian. Because interaction with the environment is limited, line-widths are correspondingly narrow.

The Hamiltonian for the rare earth ion in a crystalline host can be written as the sum of four terms each being a perturbation of the one preceding it. This is the material Hamiltonian given on page 12 and is equal

to

$$H_0 = H_1 + H_2 + H_3 + H_4 \tag{2.27}$$

where H_1 includes the kinetic term and central field potential of the nucleus, H_2 is the electrostatic potential between the electrons, H_3 is the spin orbit interaction, and H_4 is the static crystal field potential. The first three terms are associated with the free ion. The last arises from placing the ion in the host.

H_1, in the central field approximation, can be written

$$H_1 = \sum_{i=1}^{N} \left(-\frac{\hbar^2}{2m}\nabla^2_i + V(r_i)\right) \tag{2.28}$$

where $V(r_i)$ is the spherically symmetric potential each electron i sees from the nucleus. Equation (2.28) separates into N equations in electron coordinate r_i each satisfied by individual electronic wavefunctions having the good quantum numbers n, ℓ, s, m_ℓ, m_s. The energy depends only on n and ℓ giving rise to the configuration notation stating how many electrons have the same n and ℓ. The ground trivalent configuration of terbium is

$$(1s^2\ 2s^2\ 2p^6\ 3s^2\ 3p^6\ 4s^2\ 3d^{10}\ 4p^6\ 5s^2\ 4d^{10}\ 5p^6)\,4f^8$$

where that part of the configuration in parenthesis represents all closed shells. To satisfy the Pauli exclusion principle, the eigenstates are Slater determinants of the individual electronic wave functions. All states within a configuration are degenerate.

The first two perturbations are given by

$$H_2 = \sum_{i>j} \frac{e^2}{r_{ij}} \tag{2.29}$$

where the sum is over all electron pairs, and

$$H_3 = \sum_{i=1}^{N} \zeta_i (\vec{l}_i \cdot \vec{s}_i) \tag{2.30}$$

They are approximately of the same magnitude so that neither Russell-Saunders nor j-j coupling methods work very well. An intermediate approach[49] is needed involving diagonalization of $\tilde{H} \equiv H_2 + H_3$. Typically, Russell-Saunders eigenfunctions (with good quantum numbers L and S) are first used as a basis set. This diagonalizes $\tilde{H}$ in blocks of J = L+S which is a good quantum number since the free ion retains full spherical symmetry. However, final diagonalization of each block yields wave functions that are linear

combinations of the Russell-Saunders terms so that, although final free ion levels are described by the notation $(^{2S+1})L_J$, it must be remembered that L and S are no longer good quantum numbers and the values listed are those of the greatest contributing term.[52] Because the ground configuration is well isolated from the excited configurations inter-configuration interaction is small.

The final perturbation, H_4, is from the static electric field of neighboring ions and it has the same site symmetry and strength for each ion in the crystal. Dynamic interactions with the lattice or ligands are ignored. When J-mixing is small, interactions are only allowed within the $2J+1$ components (termed the manifold of J) of each individual free ion energy level. Because the full rotational symmetry is now destroyed a certain amount of splitting is expected.

H_4 is expanded in a series of spherical harmonics[53]

$$H_4 = \sum_{ikq} A_k^q r_i^k Y_k^q (\theta_i, \phi_i) \qquad (2.31)$$

where $0 \leq k \leq \infty$ and $|q| \leq k$.

The basis which diagonalizes H_4 are the vectors $|\mu\rangle$ which are linear combinations of $|\alpha Jm\rangle$ (α = those quantum numbers not listed). Depending on the site symmetry of the

ion, only those terms with certain values of q contribute to H_4. This puts a restriction on the allowed values of m used in the $|\alpha Jm\rangle$ expansion for $|\mu\rangle$. For the C_{3h} site symmetry of $Tb(OH)_3$, μ (called the crystal quantum number) takes on the values $\mu = 0, \pm 1, \pm 2, 3$. A second labeling convention is to use the label of the irreducible representation to which the state belongs. Figure (1a) shows the energy levels for $Tb(OH)_3$ and $LiTbF_4$ relevent to our experiments.

Once identification is made of how these states transform, group theoretical methods enable the selection rules for transitions to be worked out. Tables 2.2 and 2.3 give the selection rules for electric and magnetic dipole transitions for $Tb(OH)_3$ and $LiTbF_4$.

Note that pure f-f transitions are forbidden by electric dipole selection rules. However, odd parity components in the crystal field cause small amounts of configuration mixing which allow electric dipole transitions to take place. Judd-Ofelt theory[55] predicts transition intensities by using an effective transition operator formed from a tensor product of the electric dipole operator and odd parity components of the crystal field. In this model,

Selection Rules

Table 2.2 -- $Tb(OH)_3$ allowed transitions[51]

μ	0	3	-2	2	1	-1
0	mσ	eπ	$e\sigma^+$	$e\sigma^-$	$m\pi^+$	$m\pi^-$
3	eπ	mσ	$m\pi^+$	$m\pi^-$	$e\sigma^+$	$e\sigma^-$
-2	$e\sigma^-$	$m\pi^-$	mσ	$e\sigma^+$	eπ	$m\pi^+$
2	$e\sigma^+$	$m\pi^+$	$e\sigma^-$	mσ	$m\pi^-$	eπ
1	$m\pi^-$	$e\sigma^-$	eπ	$m\pi^+$	mσ	$e\sigma^+$
-1	$m\pi^+$	$e\sigma^+$	$m\pi^-$	eπ	$e\sigma^-$	mσ

Table 2.3 -- $LiTbF_4$ allowed transitions[54]

Γ	1	2	3,4
1	mσ	eπ	eσ,mπ
2	eπ	mσ	eσ,mπ
3,4	eσ,mπ	eσ,mπ	eπ,mσ

Notation: "e" refers to electric dipole transitions. "m" refers to magnetic dipole transitions. "π" refers to the electric polarization parallel to the crystalline c axis. "σ" refers to the electric polarization perpendicular to the c axis.

the effective operator acts only on states of definite parity giving nonzero intensities to intra-configurational transitions.

The parity-allowed electric dipole $4f^n$ to $4f^{n-1}5d$ transitions are quite strong in comparison with f-f transitions. Because of the extended radial wave function of the $4f^7$ 5d level, ion-host interaction becomes much larger. Thus the influence of the crystal field is greater and interpretation of the spectra of those highly excited states becomes less straightforward.

Spectral Line Broadening

As mentioned earlier, a desirable feature of rare earth doped crystals is the narrow linewidths of the resonances. Even so, spectral line broadening exists to some degree and its sources can be grouped into two categories: inhomogeneous and homogeneous broadening.

Inhomogeneous broadening in solids arises from having slightly different crystal fields at each ion, causing a spread in the ensemble of energy levels for the crystal as a whole. This can come about through crystal strains, defects, and impurities. Its signature is usually a Gaussian lineshape although non-Gaussian distributions also occur.

Homogeneous broadening, yielding Lorentzian line shapes, has four contributions[56]: (a) elastic, phase-destroying collisons, (b) inelastic collisions, (c) transitions to other levels for reasons other than (b), and (d) power broadening.

Elementary crystal excitations such as phonons and, in magnetic compounds, magnons are sources of elastic phase destroying collisions. An additional mechanism involves excitons in which the energy from the excited state of one ion is transferred to the unexcited state of a neighboring ion.[57] This occurs in $TB(OH)_3$[46,47] in the form of Frenkel excitons where the excitation is coherent and possesses a well-defined wavevector.

Phonons, magnons, and excitons can also cause inelastic collisions. Not only does this contribute to population relaxation but loss of phase coherence as well. Exciton-exciton annihilation, recently discovered in $Tb(OH)_3$ and $LiTbF_4$[58], occurs upon application of intense laser fields.

Transition to other levels for reasons other than inelastic collisions can be due to a number of causes. Spontaneous emission gives rise to the natural line width. Other cooperative processes include near resonant or intra-

line energy transfer and nonresonant or interline transfer.[59] Both cases involve phonon-assisted multipolar or exchange interactions. The intraline case occurs within a strain broadened line while the interline case occurs between different ions with energy levels differing by amounts greater than kT and/or the inhomogeneous linewidth.

In certain systems where it is favored by the energy level scheme, two-step absorption can occur. Although we were not able to conclusively measure this process in our Tb compounds,[60] it might be competing with the observed exciton annihilation processes.

Power broadening arises from stimulated emission. An exact solution of (2.4) can be derived for a two level system[61] giving a power dependent linewidth to the Lorentzian shape. For small fields it reduces to the natural line shape.

Homogeneous linewidths can be directly related to the decay constants $\Gamma_{nn'}$ of (2.5). In the absence of power broadening

$$\Gamma_{nn'} = \left(\frac{\Delta\nu_{nn'}}{2}\right)$$

where $\Delta\nu_{nn'}$ is the full width at half the maximum value of the line (FWHM). The dephasing time, or time it takes the induced dipole moment to lose its coherence due to all the above mechanisms except power broadening, is

$$(T_2)_{nn'} = (2\pi\Gamma_{nn'})^{-1}$$

Direct measurement of T_2 using a coherent transient form of FWM is described in Appendix I.

In general, both homogeneous and inhomogeneous broadening are present in line spectra; sometimes one dominates the other. Variation of different experimental parameters controls the broadening mechanisms. At low temperatures phonons "freeze out" relieving the system of such a major contribution to homogeneous broadening that inhomogeneous strain broadening plays the major role. Likewise, magnons, freeze out in applied magnetic fields. Exciton density is a function of laser power. At room temperature, phonon broadening dominates to the point where it masks information about the other, less understood, dephasing mechanisms. Thus, for our experiments, cooling with liquid helium was used, freezing out phonons leaving us with inhomogeneously broadened lines.

Chapter 3

APPARATUS AND SAMPLES

The spectroscopic system used was designed to be as universal as possible in performing optical experiments. The lasers and associated optics were mounted on optical breadboards or benches facilitating easy placement and changeability of components. Experiments requiring a magnetic field used a homemade stainless steel dewar with a superconducting solenoid while other experiments used a smaller moveable glass Dewar. The electronics had both continuous and pulsed signal capability.

The description of the apparatus which follows is divided into sections that describe the system optics, lasers, Dewars, and electronics. A short section on the samples is presented at the end.

System Optics

This section deals with the generation, manipulation, and propagation of the laser beams into the sample as well as the efficient collection of the light emitted from the sample. Figure 3.1 shows a schematic diagram of the entire spectroscopic system. The lasers can be operated individually or together and the beams directed into either Dewar (to be discussed later). The glass Dewar is easily

removable to allow collection of light from the metal Dewar by the Spex monochromator.

An important consideration in four-wave mixing experiments is to ensure that the waists (or foci) of all three input beams are of similar size and located at the input side of the crystal. Because of the differences in the positions of each of the dye lasers, this required a total of five lenses: three separate lenses at the output of each laser to give a similar conjugate waist for each beam, and two more lenses common to all three beams to define the final waist size and position at the proper place. Figure 3.1 shows values for the lenses for a typical three-beam experiment in the glass Dewar. The chosen lenses gave waists (one-half of the beam diameter) of 30-40 microns.

It should be noted that rough values for the focal lengths and positions of the lenses could be chosen on the basis of ray optics calculations in most, but not all cases. The cross-sectional profile of the dye laser beams is closely approximated by a Gaussian function; hence Gaussian beam optics[44] are more appropriate than ray optics. It is not hard to show that for $(\frac{\Pi\omega_o^2}{\lambda^2})^2 << (L-f)^2$ Gaussian beam optics reduce to ray optics and the simpler ray formulas

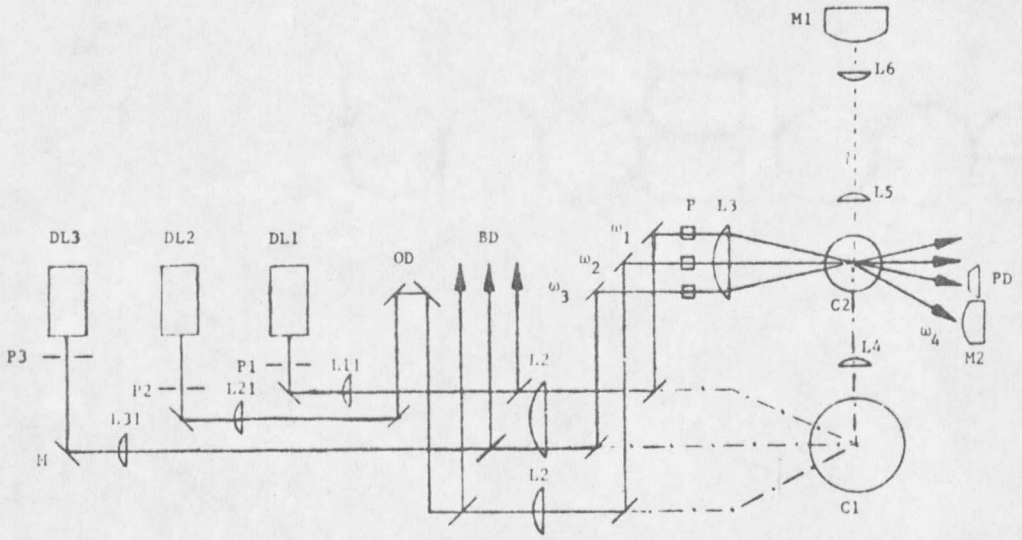

Figure 3.1. Optical system used in FWM experiments. Components are the following: DL1,2,3 -dye lasers at frequencies ω_1, ω_2, ω_3 , respectively;

OD - 79 cm optical delay
P - polarizing prisms
PD - photo diode detecting ω_1 beam absorption
M2 - MacPherson monochromator detecting ω_4 signal.
P1,2,3 -pin holes;
M - mirror or 90° prisms
M1 - Spex monochromator for fluorescence collection
C1, C2 - stainless steel Dewar, glass Dewar

Beam Optics

Lens	Focal Length	Position cm
L11	36 cm	DL1-L11:42.5
L21	57 cm	DL2-L21:58.4
L31	40 cm	DL3-L31:49.5
L2	-67 cm	DL1-L2: 95.5
L3	25 cm	L3-C2 (axis):30.5

Collection Optics

Lens	Focal Length	Position cm
L4	33.3 cm	L4-C1 (axis): 11.4
L5	5.1cm f/ 1.5	L5-C2 (axis): 6.0
L6	5.1cm	L6-M1 (slit): 5.0

Other Distances
DL1-P1:18.4 cm
DL2-P2:22.2 cm
DL3-P3:14.6 cm

may be used (ω_o = beam waist inside laser cavity, λ = wavelength, L = distance from the waist position to the lens, and f = focal length of the lens). In most situations, this was the case. However, in certain instances, notably in the index experiment discussed in Appendix II, Gaussian beam calculations were necessary.

An optical wedge was used to split off part of the beam for laser diagnostic purposes. This enabled frequency stability, pulse energy, and in the case of the mixing experiments, the relative timing of the pulses to be observed without introducing spurious Fabry-Perot behavior.[62] Fabry-Perot effects were an ever present problem and were dealt with by tilting surfaces so as to eliminate internal reflective interference or by avoiding the use of parallel optical surfaces altogether.

Absorption data were taken in either of two ways: using a tungsten-halogen lamp and scanning the monochromator, or scanning a narrow-band dye laser with a spectrally insensitive detector such as a photodiode or the monochromator with wide slits.

The optics for the laser absorption were as depicted in Figure 3.1. The ω_1 beam absorption was monitored at the exit window of the dewar simultaneously with

the four-wave mixing signal allowing exact spectral synchronization of the signal with the absorption. This both avoided problems related to laser drift and speeded up the accumulation of data.

The monochromators used included a Spex Model #14018 0.85-meter Czerny-Turner Double Monochromator with two 1800 groove/mm holographic gratings and a McPherson Model #218 0.3 meter monochromator with a 1200 l/mm grating blazed at 5000 Å.

Fluorescence collection was achieved by observing the side profile of the laser beam going through the crystal. In some cases, this was adequate. However, in highly absorbing crystals such as the ones in these experiments, distorted line shapes occurred. In such situations a back scattered collection geometry is better. More will be said about this later.

Lasers

Two homemade nitrogen lasers generating 10 nsec pulses pumped up to three tunable dye lasers. One, a single beam model, pumped the ω_1 laser with a peak power of 550 kW. The other, a double-beam model, pumped the ω_2 and ω_3 lasers with a total (double-beam) power of 580 kW.

The three dye lasers were of the Hänsch type[63]

with one of them (ω_1 laser) operating in the high resolution, etalon-narrowed, oscillator-amplifier mode to give a 45 kW beam with 0.03-0.05cm^{-1} linewidth. This was the laser that was scanned through the $^5D_4$ transition. Dye laser pulses lasted 5 nsec.

Dewars and Dewar Optics

Two separate dewars were used throughout the experiments. The metal one housed a 60 kG superconducting solenoid built by American Magnetics, and was used for initial survey experiments with and without magnetic fields. The glass dewar, purchased from Pope Scientific, was used during the later stages of data taking.

Because of the difficulty in determining the waist positions of the beams relative to the sample inside the dewar, a pair of orthogonal razor blades placed on an X-Y translation mount was located at a conjugate sample position outside the dewar. Sending the beams to the blades via a removable mirror enabled not only the waists to be put in their proper position but also allowed adjustments to be made to ensure the beams were crossed at the waist position.

Electronics

An important consideration of the mixing experi-

ments involved firing the lasers at the same time or, in other cases, providing for a variable delay between the firing of the ω_1 laser and the firing of the ω_2 and ω_3 lasers. To gain this capability, Douglas Jones designed the electronic trigger and delay unit used to trigger the two nitrogen lasers. Pulse jitter was less than one nanosecond. Laser repetition rates used were $3^1/_3$ pps during early experiments and 10 pps during the final ones.

The signals from the photomultiplier tubes collecting light from the monochromators were sent to either a Keithley 416 picoammeter or a Princeton Applied Research 162 boxcar averager (or both in the case of the synchronized absorption and mixing experiments). Data was then temporarily stored on a Northern Scientific 575 multichannel analyzer, then transferred and stored on disks via a CRDS MF-211 computer (DEC LSI 11).

Samples

The experiments were carried out on several different samples of the compounds $Tb(OH)_3$ and $LiTbF_4$.

The $Tb(OH)_3$ crystals, obtained from Professor Werner Wolf, were grown using a hydrothermal technique[64] developed by H. E. Meisner of Yale University. They grow in the form

of a hexagonal needle parallel to the c axis and are small, being on the order of 2 mm long and 250 to 350 μm thick. There are two ions per unit cell with C_{3h} point symmetry.[65,66]

The $LiTbF_4$ crystals were cut from a boule obtained from H. J. Guggenheim of Bell Laboratories, Murray Hill. The sample used in the mixing experiment was oriented, cut, and polished by Mark Ritter in the shape of a rectangular prism of dimensions 0.55 x 1.04 x 3.61 mm. The long dimension is parallel to the c axis. $LiTbF_4$ has four ions per unit cell with S_4 point symmetry.[67,68] The damage threshold was empirically measured to be 875 MW/cm^2.

Chapter 4

RESULTS AND DISCUSSION

As discussed in Chapter 1, the initial observation of the FWM signal raised two major questions. The first dealt with the exact nature of the nonlinear process itself. The second involved explaining the narrowed lineshape and its location within the absorption profile. An additional complication arose upon the observation of a splitting in the fluorescence excitation of the $^7F_6 - {}^5D_4$ transition when none was observed in the absorption. See Figure 4.1. Determination of the relationship (if any) between the splitting and the FWM signal needed to be made

Because most of the experiments were done with two input beams of frequencies ω_1 and ω_3 rather than the more general case of three input beams, subsequent discussion will deal with the two beam case (we have $\omega_4 = 2\omega_1 - \omega_3$ for $\omega_2 = \omega_1$). Exceptions will be noted.

Nature of Signal

The ω_4 signal was detected upon application of two beams of frequencies ω_1 and ω_3 while ω_1 was scanned through the intermediate resonance $|b\rangle$ of Figure 2.1(a). Crystal temperature was 1.3 K. The fact that light mixing was

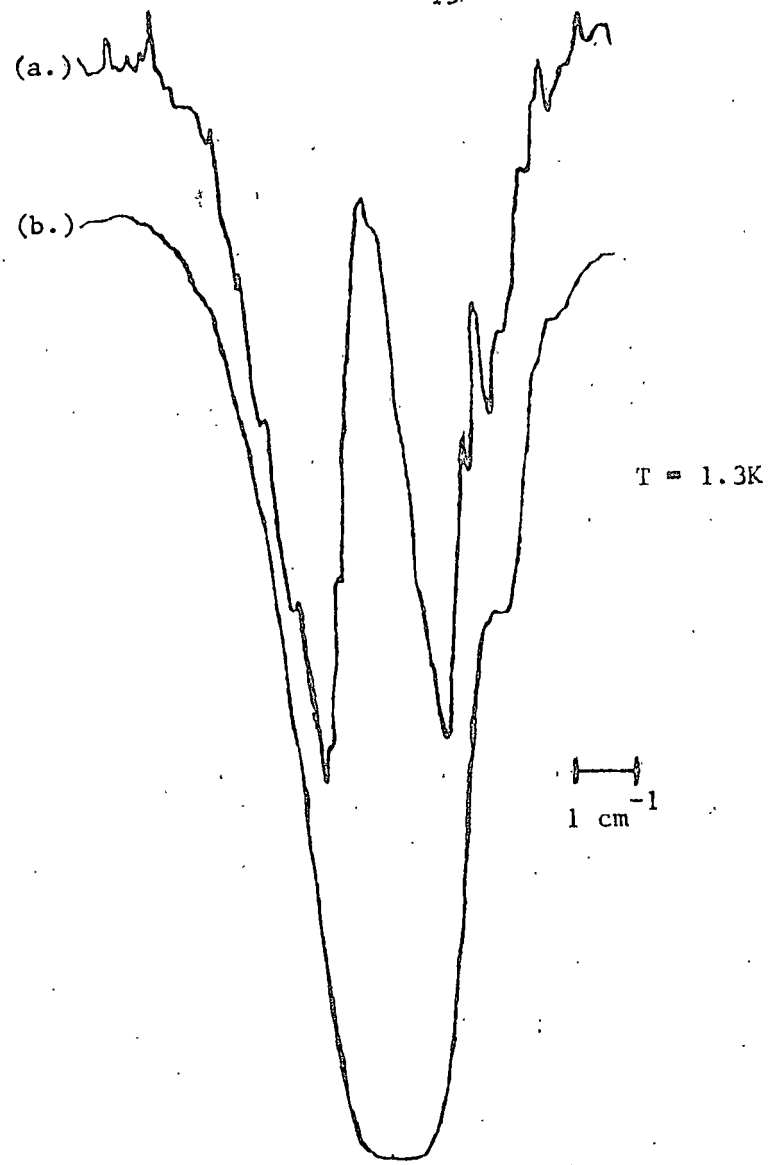

Figure 4.1. (a.) Fluorescent excitation spectrum showing splitting $^5D_4$ $\mu=3^+$ state. B = 50kG. Splitting was also observed in $LiTbF_4$. Spectrum was taken by scanning ω_1 through resonance while monitoring the fluorescence intensity. (b.) Corresponding absorption.

occurring, the necessity for temporal and spatial overlap of pulses, and the directionally distinct ω_4 output all strongly suggested a third order nonlinear interaction such as CARS or TPAFWM.

Nevertheless, other processes could account for these observations. They include the two-step process involving $\chi^{(2)}$ or higher order processes[69] of $\chi^{(n)}$ for $n \geq 3$.

The higher order processes may be ruled out on the basis of the observed dependence of the signal intensity on the power of the input beams. From equation (2.9), the intensity dependence of ω_4 signal on the input beam intensities for any particular order can be determined. Thus, for a third order process, the sum of the powers of the input intensities is three. A fourth order process sums to four, etc. Figure 4.2 shows the power of the ω_4 signal as a function of the ω_1 beam power and ω_3 beam power respectively for the two-beam experiment. We find a quadratic dependence for the ω_1 power and a linear dependence for the ω_3 power. We thus have $n \leq 3$.

The two-step second order process can be eliminated as a possibility by symmetry considerations. For all experiments (unless otherwise noted), both input beams

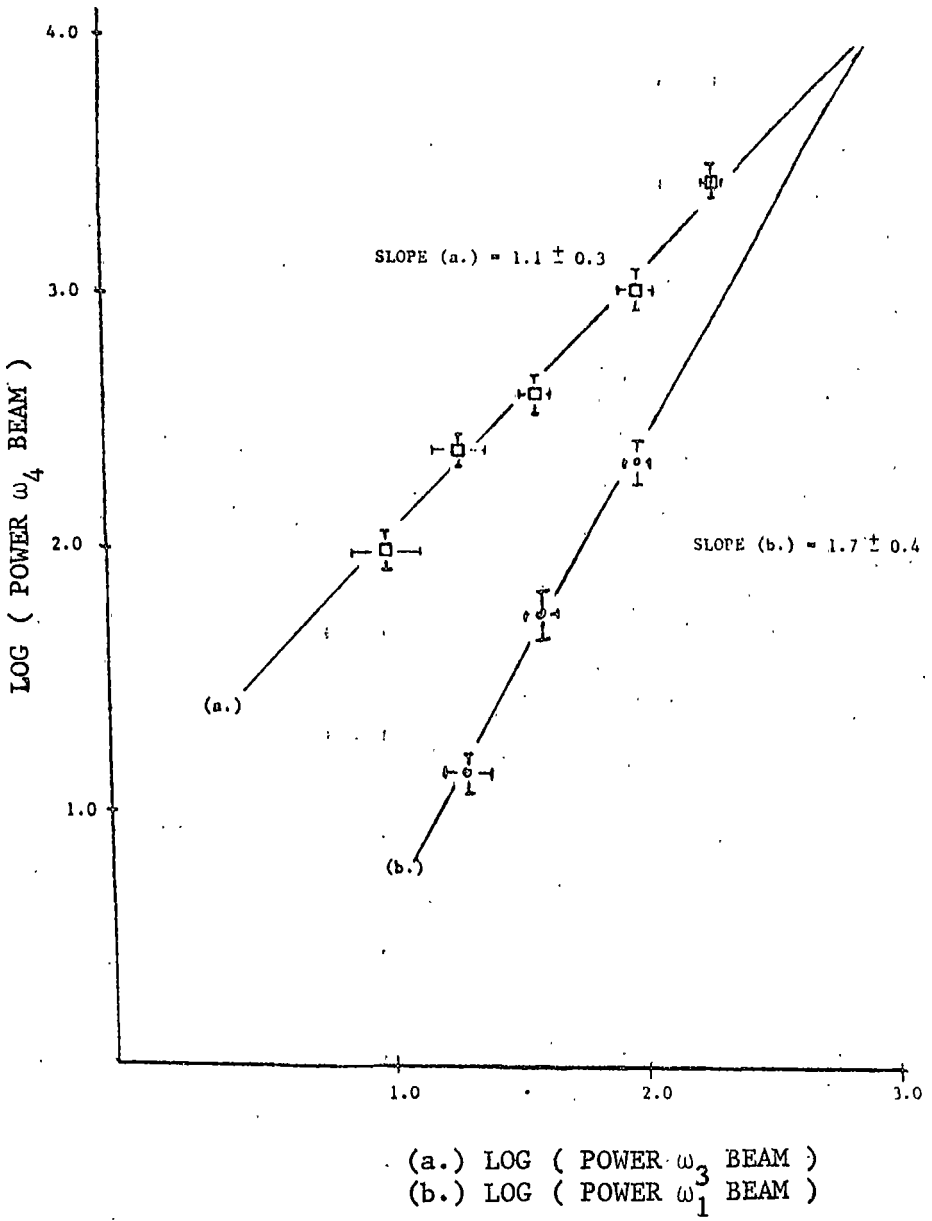

Figure 4.2. Log (signal power) as a function of log (input power) for (a.) ω_3 beam and, (b.) ω_1 beam, in 2-beam experiment in $Tb(OH)_3$.

and signal were Π polarized ($\vec{E}$ parallel to c axis). $\chi^{(2)}_{izz}$ vanishes for both C_{3h} ($Tb(OH)_3$) and S_4 ($LiTbF_4$) point symmetries for all i.[70] Therefore, the second order process cannot occur, and we are left with only $\chi^{(3)}$ as the mixing mechanism.

A CARS signal can also be discounted as it would have a strong $(\omega_1 - \omega_3)$ dependence. Figure 2.1C shows the relevant energy level diagram. If CARS were involved, choosing different values for ω_3 would move $(\omega_1 - \omega_3)$ in and out of resonance with states in the ^7F_J manifolds, thereby changing the signal strength. No such change was observed. As a further precaution, ω_1 and ω_3 were chosen to avoid any Raman resonances. These were obtained from spontaneous electronic and phonon Raman spectra measured previously and from Table 4.1, which lists the electronic energy levels of the ^7F term. Unless otherwise noted, ω_3 was chosen to be 18301 cm^{-1} for $Tb(OH)_3$ and 17422 cm^{-1} for $LiTbF_4$.

The elimination of the above third order processes focused our attention on TPAFWM. Examination of selection rules showed that $\chi^{(3)}_{zzzz}$ is allowed under the C_{3h} and S_4 point symmetries of $Tb(OH)_3$ and $LiTbF_4$.[70] As seen from equation (2.10), electric dipole selection rules operate

Table 4.1

^7F_J Energy Levels

(a) $Tb(OH)_3$ at 4.2K,[51] experimental values in cm^{-1}

J	μ	Energy	J	μ	Energy
6	0+	0.0	4	3+	-
	0-	0.0		2	3476.1
	1	118.2		3-	3473.1
	2	206.0		0	3483.4
	0+	224.4		1	3539.2
	1	233.7		2	3600.7
	3+	-			
	2	252.3			
	3-	-			
5	3-	2082.0	3	1	4428.6
	2	2143.9		3-	4478.8
	1	2170.9		2	4485.2
	3+	2229.1		0	4484.3
	2	-		3+	4540.5
	1	2323.9			
	0	-			

$^7F_2 - {}^7F_0$ manifolds undetermined.

(b) $LiTbF_4$ [68] at 10K, theoretical values in cm^{-1}

J	μ	Energy	J	μ	Energy
6	2	0	4	1	3325
	2	2		2	3399
	3,4	108		3,4	3400
	1	119		1	3539
	2	135		2	3572
	3,4	175		3,4	3630
	1	223		1	3845
	1	376			
	3,4	390	3	2	4324
	2	401		3,4	4404
				1	4478
5	2	2087		3,4	4528
	3,4	2089		2	4536
	1	2130			
	1	2148	2	1	5024
	3,4	2162		2	5064
	1	2339		3,4	5285
	3,4	2390		2	5371
	2	2403			
			1	1	5603
				3,4	5714
			0	1	5923

in a step-wise fashion for the transitions associated with χ_{res}. Tables 2.2 and 2.3 show that electric dipole transitions are allowed between states $|a\rangle$ and $|b\rangle$ of Figure 2.1 (a) for the quantum numbers involved in our experiments. In order to determine if multiresonant enhancement was taking place, Paula Fisher took linear UV absorption scans on both $Tb(OH)_3$ and $LiTbF_4$. Her results are given in Figure 4.3. They indicate that $2\omega_1$ falls in the broad $4f^7 5d$ absorption band.[71] Because the mixing process utilizes an intermediate $4f^8$ state, the strong parity allowed transition to the $4f^7 5d$ band provided major enhancement to the mixing.

To gain final confirmation of the two-photon resonant nature of the FWM spectra, a three-beam mixing experiment was performed in which ω_2 was tuned away from ω_1. The results, shown in Figure 4.4 indicate (a) that signal enhancement of over twenty-five times is available by choosing $(\omega_1 + \omega_2)$ to fall on resonance in the three-beam experiment, and (b) the upper energy wing of the two-photon resonance is utilized in the two-beam experiment in which $\omega_2 = \omega_1$. We have thus identified the FWM as doubly-resonant, two-photon-absorption-induced FWM. The two-photon resonance has important applications to be discussed

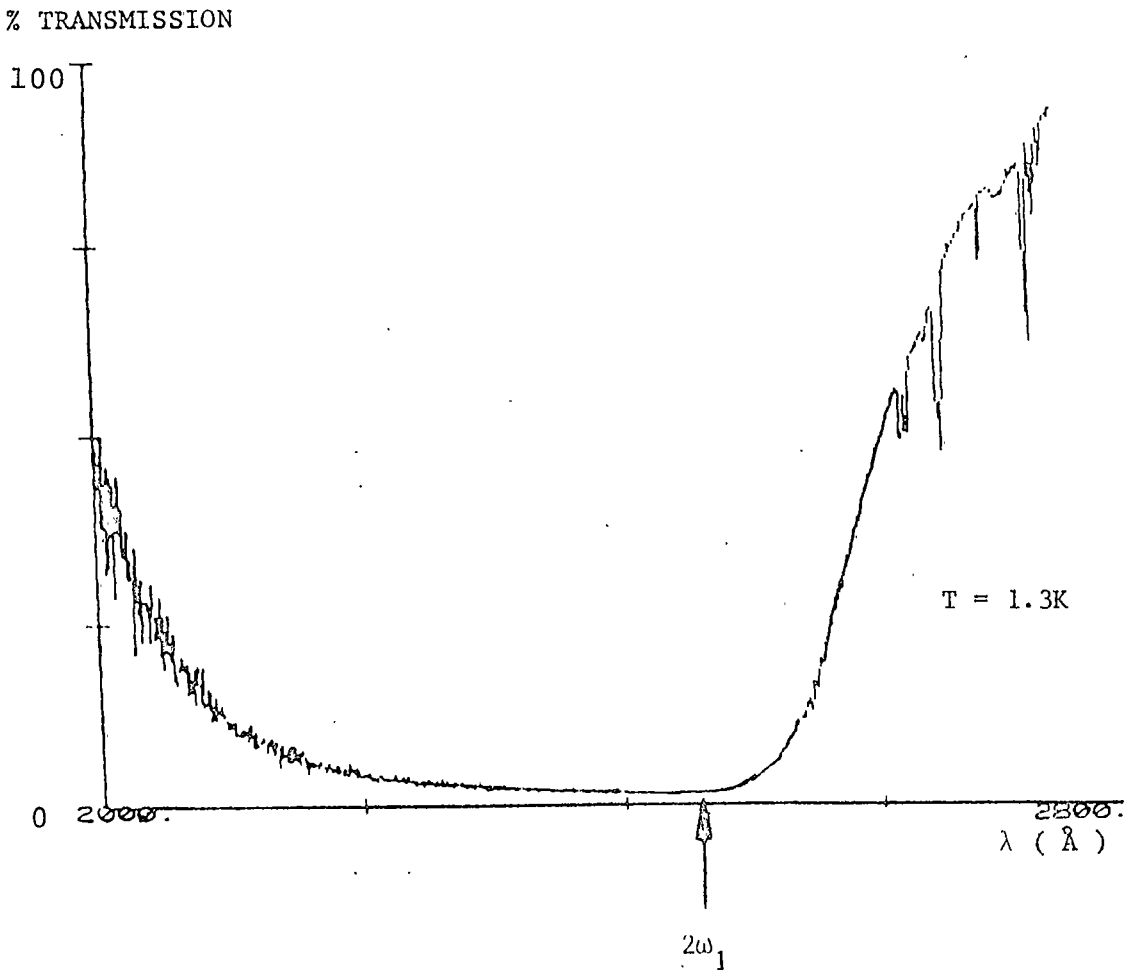

Figure 4.3. Broad linear UV absorption band in $Tb(OH)_3$ associated with excited state in TPAFWM.

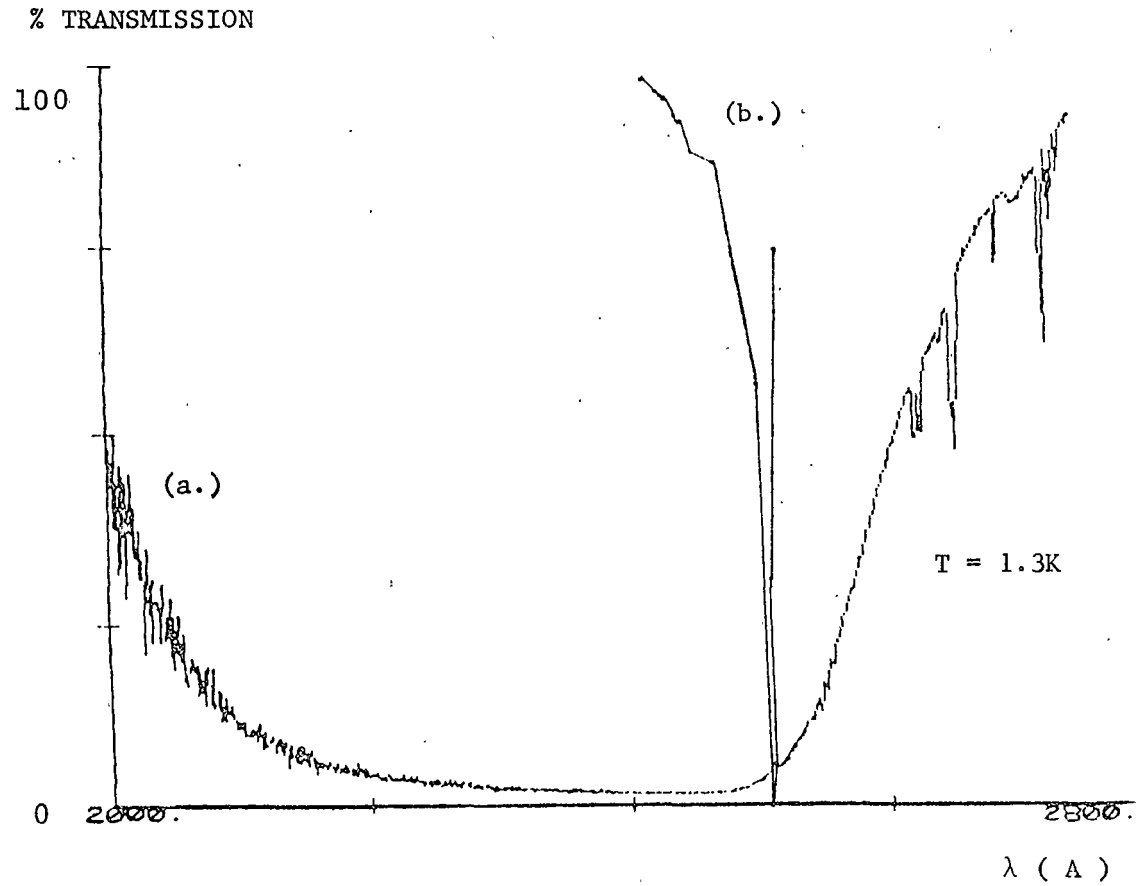

Figure 4.4. (a.) Broad $4f^7 5d$ absorption band, $Tb(OH)_3$, and (b.) resolved crystal field component using TPAFWM.

later.

Line Narrowing

Upon first observation of the line narrowing, we were faced with consideration of several possible explanations. To begin with, crystal defects could cause narrowing by giving rise to broken symmetries. This would enable different selection rules to operate in different parts of the inhomogeneous distribution, thus favoring one section over the other. If this were the case, sensitivity to samples obtained from different batches would be possibly exhibited. None was seen for $TB(OH)_3$.

Second, narrowed lines approximating homogeneous linewidths can be obtained under certain conditions using special resonances in the susceptibility.[73] However, such conditions are of limited generality and did not apply to our experiment.

Third, the FWM could be narrowed by using a selection rule favoring only one side of the splitting obtained in the fluorescent excitation spectrum of Figure 4.1. While this explanation was discounted by other observations, a splitting may play a role in explaining the finer details of our data. This will be discussed shortly.

Finally, it should be mentioned that interference effects between resonant and nonresonant contributions to the susceptibility may lead to dispersive-like lineshapes.[42] Although this would not significantly narrow the lines, it could complicate the determination of the actual line narrowing mechanism. Fortunately, in our case, the nonresonant background was much less than the resonant signal thereby minimizing the interference.

In order to pin down the cause of the narrowing, all experimental parameters were systematically varied. It was found that the major variable affecting both the spectral position and shape of the ω_4 signal within the inhomogeneous absorption was the beam crossing angle inside the sample. See Figure 4.5.

None of the above explanations can account for this observed angle dependence. Instead, the following qualitative model has been developed, based upon the inclusion of the dispersive nature of the index of refraction on the phase matching conditions. In all other treatments of phase matching, anamalous index dispersion has been ignored.

From equation 2.26, we have $k_1 = \omega_1 n_1/c$. We can treat $\alpha_3 = \alpha_4 \underset{\sim}{} 0$ so that for all beams Π polarized in the two-beam experiment, equation (2.23) becomes

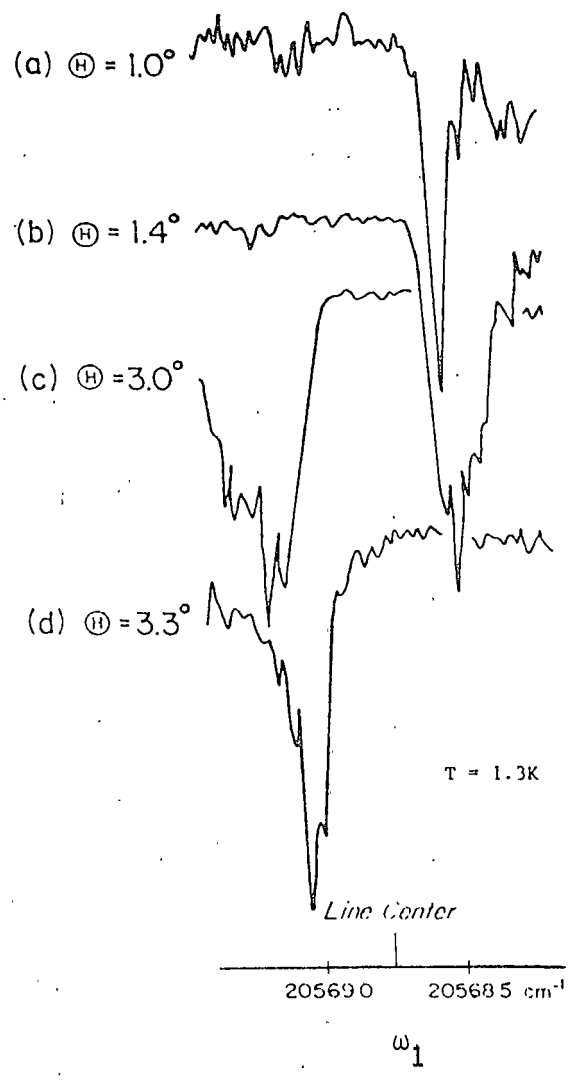

Figure 4.5. Four-wave mixing signal at ω_4 as a function of ω_1 for several internal beam crossing angles θ in $LiTbF_4$. ω_3 = 17422 cm^{-1}.

$$I_{4Z} \propto |\chi^{(3)}_{ZZZZ}(\omega_4)|^2 I^2_{1Z}(0) I_{3Z}(0) [1+\exp(-2\alpha_1 L) - 2\exp(-\alpha_1 L)\cos(\Delta k\, L)]/(\Delta k^2+\alpha_1^2) \quad (4.1)$$

where $\Delta\vec{k} = (2k_1 - k_3) - k_4$, the degree of phase mismatch. Scanning ω_1 through resonance changes Δk in two ways. It depends directly on ω_1 and can change indirectly through the dispersive nature of $n_1(\omega_1)$. For spectral lines with small widths, the first way is insignificant. The second way, however, becomes important when scanning through a resonance.

The intensity of the ω_4 signal drops off in those areas of the resonance where the dispersive change in the index rules out phase matching; a narrowed signal results. The position of the signal within the inhomogeneous line is determined by $n_i(\omega_i)$, while the width of the signal is governed by $dn_i/d\omega_i$. In situations where $dn_i/d\omega_i$ is steep enough, the narrowing is limited only by the homogeneous width of the transition.

Figure 4.5 shows the data obtained by monitoring the intensity of the ω_4 signal while the ω_1 beam was scanned through the $^5D_4$ state. Four different internal crossing angles are shown. Note that the signal is much narrower than the corresponding white-light absorption coefficient of

Figure 4.6 (a) which is expected to give a measure of the shape of the inhomogeneously broadened $\chi^{(3)}$.

As the internal crossing angle θ increases from 1.0° to 1.4°, the value of k_1 which satisfies the phase matching condition shrinks, and the signal moves to the low energy side of the transition. It also broadens consistent with moving toward a flatter part of the index dispersion curve. Increasing the angle from 1.4° to 3.0° drives the line to the high energy side of the absorption profile as phase matching occurs for smaller index. Finally, increasing θ to 3.3° pushes the signal more toward line center and narrows it corresponding to the steeper index region.

Additional observations have been made which reinforce the index model. By holding the crossing angle fixed and tuning ω_3, results are obtained similar to those involving changes of angle. The narrowed line can again be driven from one side of the transition to the other as would be expected due to changes in phase matching (see Figure 4.7). In $Tb(OH)_3$, for θ = 4.4°, narrow lines occur on the high energy side of the $^5D_4$ ω_1 resonance when ω_3 = 18301 cm^{-1} and occur on the low energy side of the ω_1 resonance when ω_3 = 16900 cm^{-1}. Finally we note that a

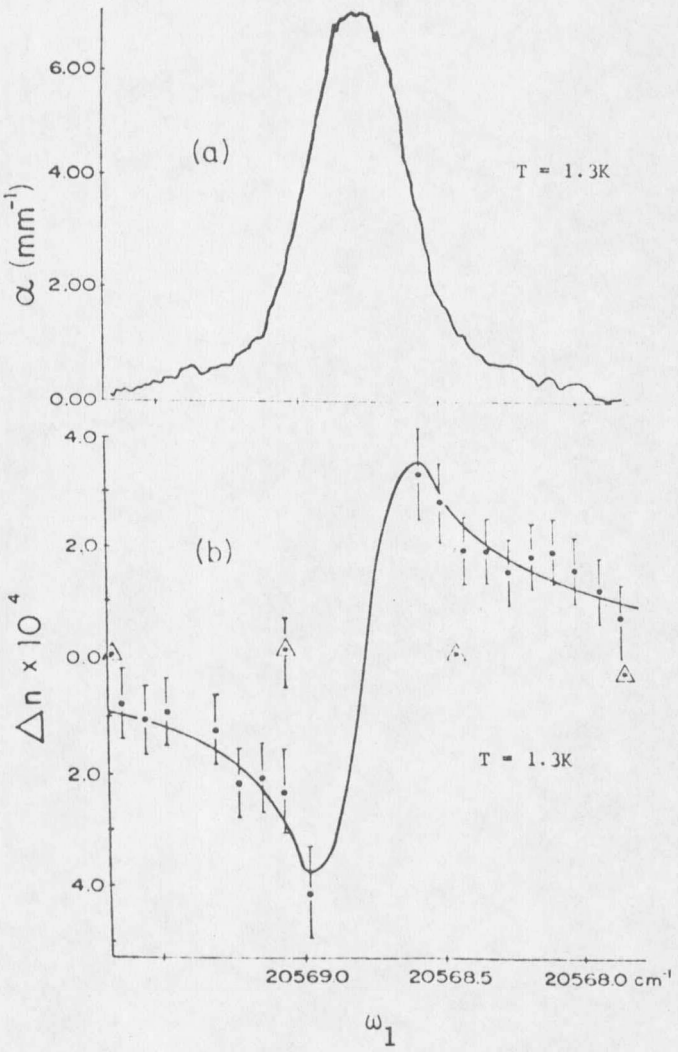

Figure 4.6. (a) White-light π polarized absorption coefficent for $^5D_4$ Γ_1 state of $LiTbF_4$ taken with 0.1 cm^{-1} resolution and (b.) index of refraction of the same state. Crystal data: dots; control data with crystal removed: dotted triangle. The single error bar on the control point is typical. The horizontal axis is the same for both graphs.

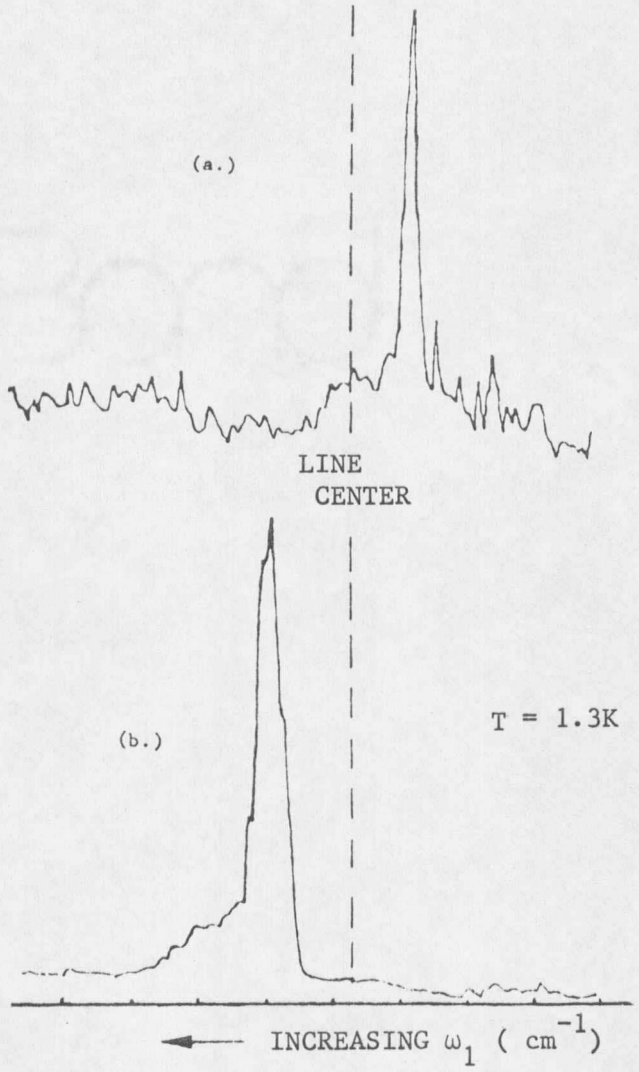

Figure 4.7. Dependence of FWM signal on ω_3. Internal crossing angle fixed at $\theta = 4.4°$. (a.) ω_3 = 16900. (b.) ω_3 = 18301. $Tb(OH)_3$.

complete set of phase matching versus angle data has been obtained on the $^5D_4$ $\mu = 3^+$ state of $Tb(OH)_3$ (Figure 4.8) and that narrowed lines have been observed on other transitions in both compounds.

While good qualitative agreement is obtained from the index model, it must be realized that present day nonlinear optical theory is severely taxed to include a full description of all the interactions actually occurring. Intrinsic phenomena such as exciton behavior, pump depletion, inhomogeneous broadening, and higher order effects in the refractive index may all need to be considered. Experimental parameters such as finite laser band widths and power broadening might also be important.

In spite of all this, an attempt was made to quantitatively check the above model. Direct measurement of the linear index of refraction as ω_1 scanned through resonance was made. A description of the experiment is given in Appendix II. The results are shown in Figure 4.6 (b). The measurements of the index and white light absorption provided the necessary parameters to plot equation (4.1). For convenience, a Lorentzian lineshape for α was used. This avoided numerical integration (to be discussed shortly).

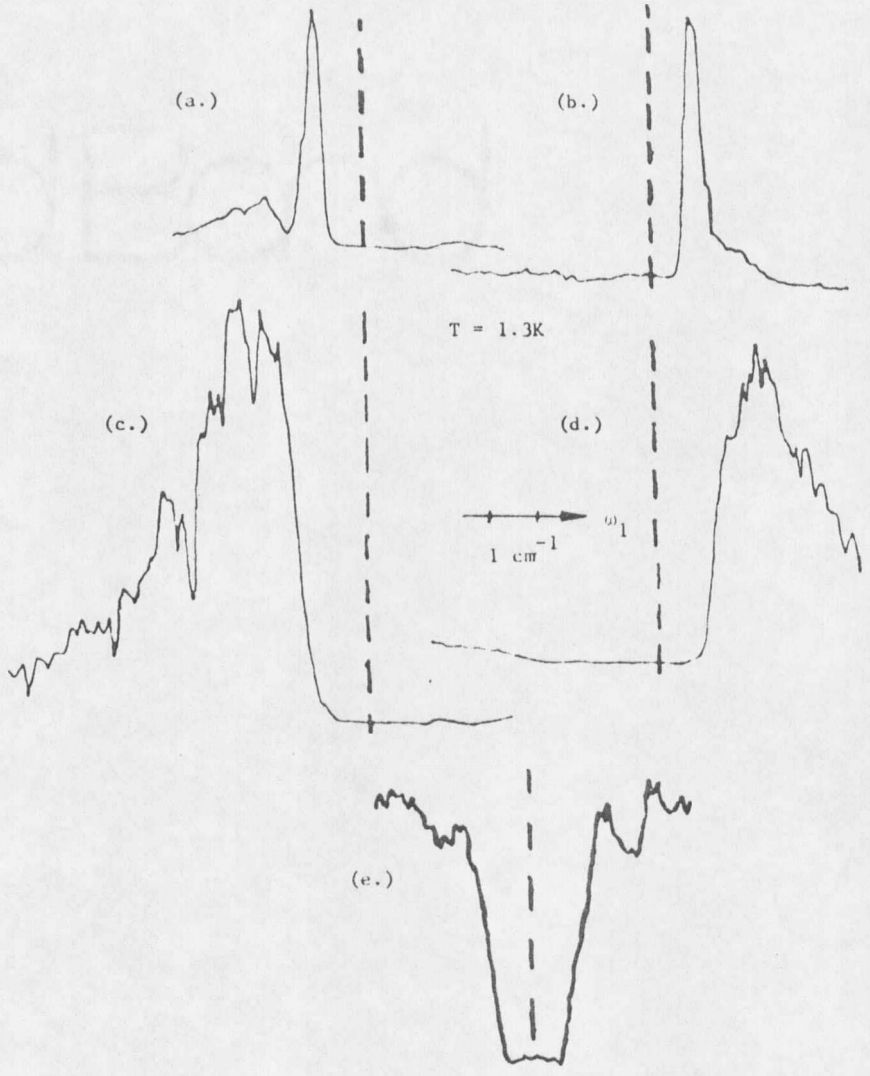

Figure 4.8. FWM signal at ω_4 for different internal angles θ in $Tb(OH)_3$. Dashed lines refer to line center. ω_3 = 18301 cm^{-1}. (a.) θ = 1.6°, (b.) θ = 4.4°, (c.) θ = 2.5°, and (d.) θ = 3.5°. (e.) corresponding absorption.

The simulation, shown in Figure 4.9, indicates that the magnitude of Δn is only great enough to distinguish between the top and bottom of the dispersion curve, moving the signal from one side to the other upon change of angle but giving linewidths much too large.

In Figure 4.10 we increase the magnitude of Δn by a factor of 3.8. Here we get the correct spectral motion of the signal along with the appearance of a distinct central peak resulting from phase matching occurring on the inside portion of the dispersion curve. The signals are still wider than those measured.

Finally, Figure 4.11 shows the effect of greatly increasing n by 35 times. The spectral narrowing of the signal (on the outside part of resonance) is now equal to that of the narrowest line we have measured (approximately the laser linewidth). Assuming that the $n_1(\omega_1)$ measurements are accurate, this leads to the possibility that $\chi^{(3)}$ is adding to the linear index of refraction in the mixing experiments.

Note that the above model is highly sensitive to the magnitude and probably the shape of absorption and index profiles. Comparison of Figures 4.12 and 4.13 with Figure

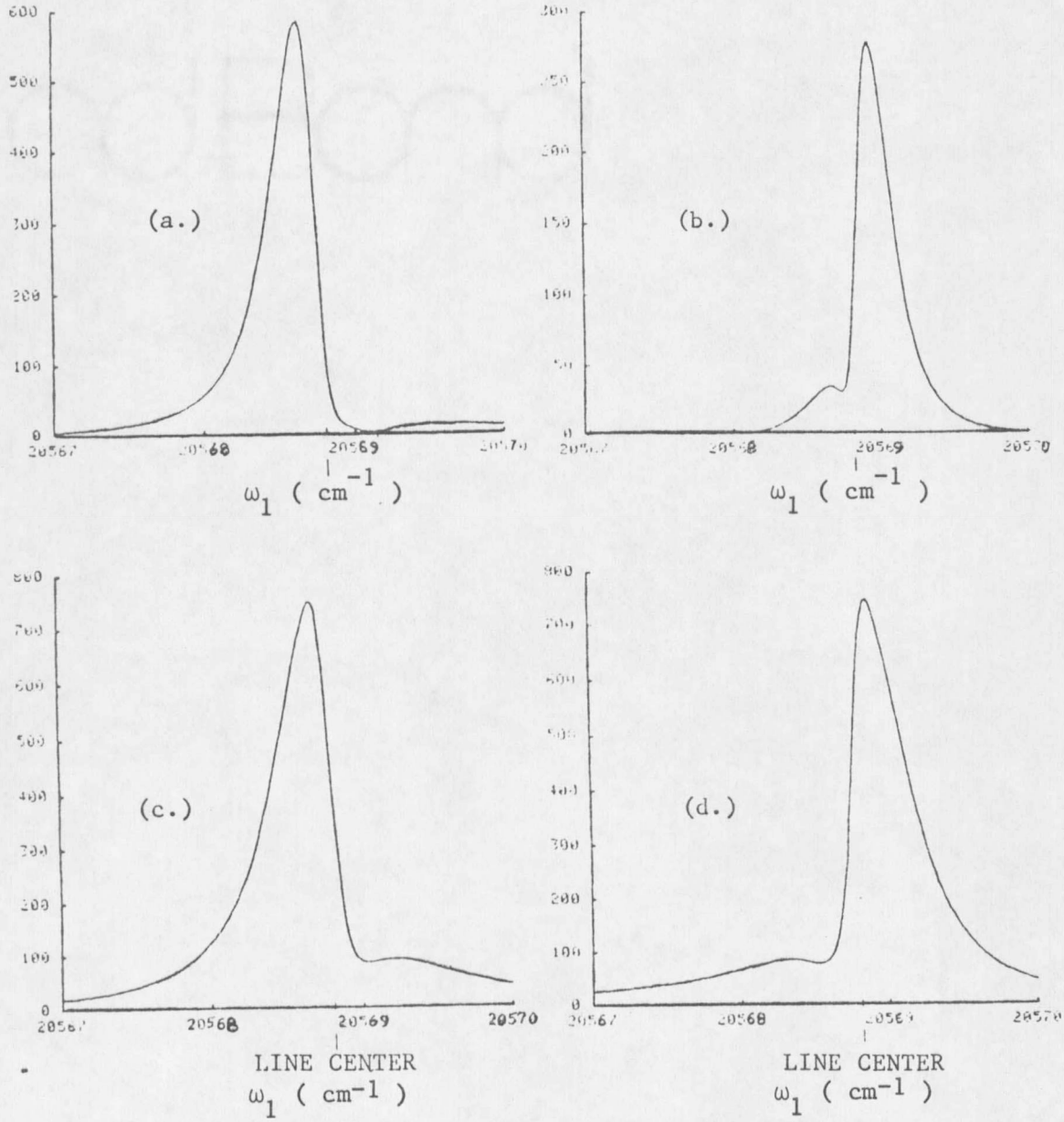

Figure 4.9. Computer simulation of equation 4.1 for 4 different crossing angles. (a.) θ = 1.25°, (b.) θ = 3.0°, (c.) θ = 1.75°, and (d.) θ = 2.5°.

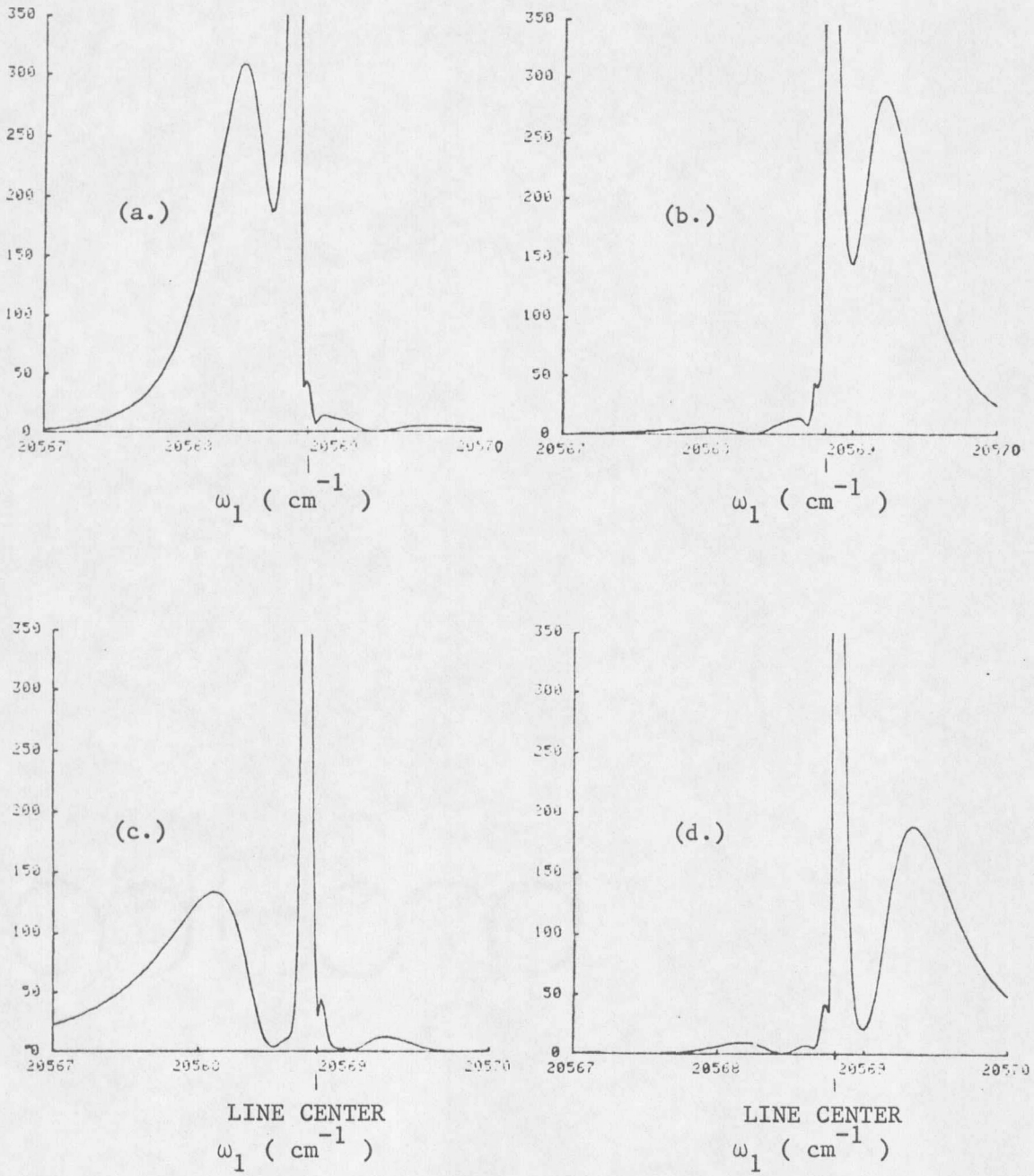

Figure 4.10. Computer simulation of equation 4.1 with Δn increased by 3.8. (a.) $\theta = 0.0°$, (b.) $\theta = 3.3°$, (c.c) $\theta = 1.5°$, (d.) $\theta = 2.8°$.

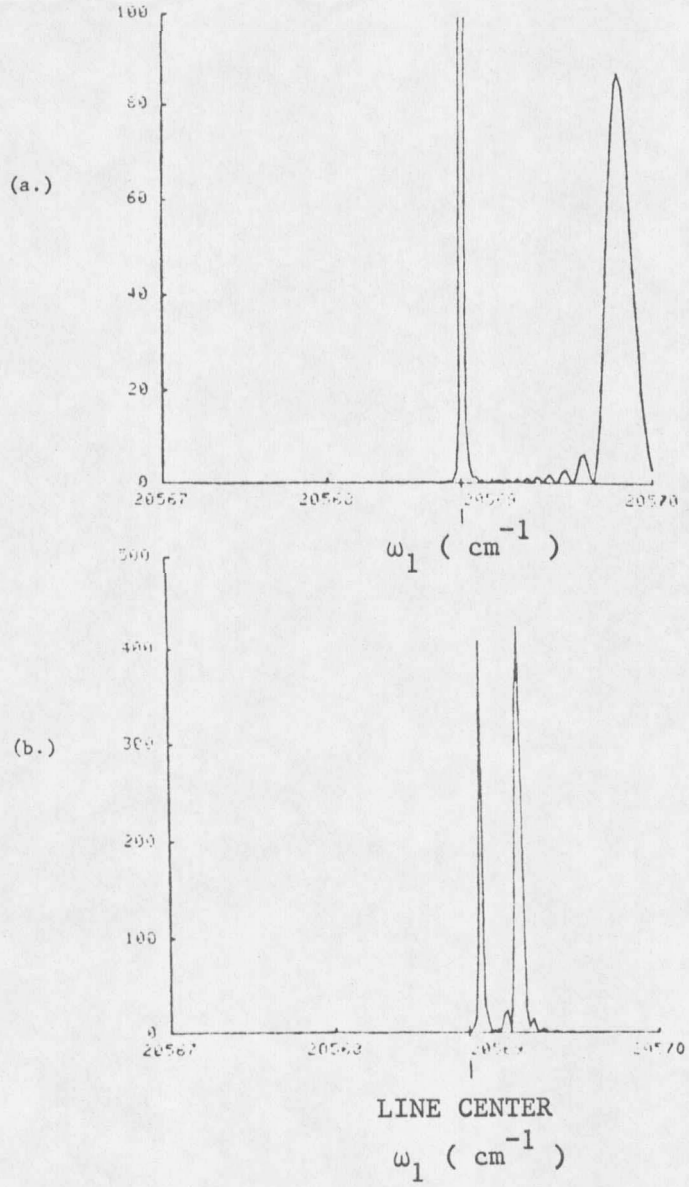

Figure 4.11. Computer simulation of equation 4.1 with Δn increased 35 times. (a.) θ = 5.5°, and (b.) θ = 8.0°.